Chemistry, Physics and Technology of Surface. 2014. V. 5. N 4. P. 361-385

PACS: 61.43.Gt; 68.08.-p; 68.35.Md; 68.43.−h

V.M. Gun'ko [1], V.V. Turov [1], V.I. Zarko [1], O.V. Goncharuk [1], O.S. Remez [1], R. Leboda [2], J. Skubiszewska-Zięba [2]

INTERFACIAL BEHAVIOR OF LOW- AND HIGH-MOLECULAR WEIGHT COMPOUNDS *VS.* TEMPERATURE AND CONFINEMENT EFFECTS

[1] Chuiko Institute of Surface Chemistry of National Academy of Sciences of Ukraine
17 General Naumov Str., Kyiv, 03164, Ukraine, E-mail: vlad_gunko@ukr.net
[2] Maria Curie-Skłodowska University, Faculty of Chemistry
3 Maria Curie-Skłodowska pl., Lublin, 20031, Poland

The interfacial and temperature behavior of water, n-decane, decanol, poly(dimethylsiloxane) (PDMS) bound to nanooxides initial or after high-pressure cryogelation and silica gels was analyzed using low-temperature ^{1}H NMR spectroscopy (applied to static samples to observe only mobile adsorbates), differential scanning calorimetry (DSC), thermoporometry and quantum chemical methods. Both NMR and DSC results demonstrated that during heating of frozen samples a fraction of organics or PDMS remained frozen at temperature higher than the melting point of bulk liquid and a fraction of any adsorbate remained unfrozen upon cooling at temperature lower than the freezing point. These effects depend on the type of an adsorbate and the pore sizes of an adsorbent. Broadening of freezing/melting temperature range is observed for PDMS or decane confined in pores of silica gel or voids between nanoparticles in fumed nanooxides. This effect is minimal for silica gel Si–100 with broad mesopores.

***Keywords**: nanooxides, silica gels, cryonanooxides, interfacial phenomena, confined space effects, freezing point depression, cooling/heating, hysteresis effects*

INTRODUCTION

Interfacial behavior of low- and high-molecular weight compounds at a surface of solid adsorbents depends on several factors such as textural characteristics and surface chemistry of adsorbents, adsorbate characteristics (molecular weight, chemical structure, polarity, polarizability), presence, type and content of co-adsorbates, medium characteristics (polarity, molecular weight of solvent molecules), temperature, heating or cooling rate, *etc.* [1–7]. These phenomena are of interest from both theoretical and practical points of view since this behavior is connected to the efficiency of adsorbents used in various media in different applications.

The interfacial phenomena are characterized by relatively complex dependences on temperature and a heating or cooling rate [7–18]. Previously, the interfacial behavior of water with a set of low- and high-molecular weight co-adsorbates was studied at a surface of oxide adsorbents using low-temperature ^{1}H NMR spectroscopy, NMR cryoporometry, calorimetry, thermoporometry, relaxometry, thermally stimulated depolarization current, dielectric relaxation spectroscopy and other methods [7–18]. It was shown that interfacial water could be divided into four types [7]. The first one is strongly bound water (SBW) characterized by significant changes in the Gibbs free energy ($-\Delta G > 0.5$–0.8 kJ/mol) due to strong interaction with an adsorbent surface, and this water can be frozen at $T < 255$–260 K. The second type is weakly bound water (WBW) characterized by smaller changes in the Gibbs free energy ($-\Delta G < 0.5$–0.8 kJ/mol) due to weaker interaction with an adsorbent surface than SBW, and it can be frozen at 255–260 K $< T < 273$ K. The third type is strongly associated water (SAW) characterized by chemical shift of the proton resonance $\delta_H = 3$–5 ppm close to that for bulk liquid water (4.5–5.5 ppm). The fourth type is weakly associated water (WAW) characterized by $\delta_H = 1$–2 ppm which represents small 3D clusters or strongly branched 2D clusters or 1D clusters or individual water molecules in hydrophobic surroundings. The presence of different waters at

the interfaces depends on the types of adsorbent and dispersion medium, porosity and structure of the adsorbent, content of water, and type and content of a co-adsorbate or a solute [7–18]. Confinement effects play an important role in the interfacial behavior not only of water but also of other adsorbates and solutes [7–18]. Therefore, here we analyze the confined space effects on the behavior of low- (water, decane, decanol) and high-molecular (poly(dimethylsiloxane), PDMS) compounds bound to nonporous nanoparticles of fumed oxides or located in pores of different silica gels. Besides low-temperature ^{1}H NMR spectroscopy, differential scanning calorimetry (DSC), nitrogen adsorption-desorption, and quantum chemistry methods are used to analyze the mentioned phenomena. The characteristics of silica gels, nanooxides, and cryonanooxides are analyzed mainly with respect to expected confined space effects. Adsorption and interfacial behavior of low-molecular weight compounds is studied to analyze weakly and strongly bound fractions of them with additional consideration of the effects of salt ions, micro- and nanocrystallites. Adsorbed decane and PDMS under confined space effects are studied to elucidate features of interfacial phenomena upon cooling-heating giving the hysteresis effects.

MATERIALS AND METHODS

Materials. Silicone oil (poly(dimethylsiloxane), PDMS) Oxane 1000 (Opsia, Labege Cedex, France, viscosity ~1000 cSt, molecular weight 44–45 kDa, polymerization order ~600, crystallization temperature ~184 K), silica gels Si–40, Si–60, and Si–100 (Merck) with beads of 0.2–0.5 mm in diameter, and pyrogenic silicas (nanosilicas) PS400 (S_{BET} = 409 m^2/g), PS300 (S_{BET} = 297 or 302 m^2/g) and PS100 (S_{BET} 84 m^2/g) (pilot plant of Chuiko Institute of Surface Chemistry, Kalush, Ukraine) were used here without specific treatments in contrast to cryonanooxides [17, 18]. To study the interfacial behavior of PDMS alone or bound to a silica surface depending on temperature, different silicas were selected with relatively close mesoporosity. Before NMR measurements, the silicas were heated at 520 K to remove adsorbed water, and then the samples were cooled to room temperature and certain amounts of PDMS were added. Residual amount of water bound to silicas was smaller than 0.5 wt. %. Selected portions of water or other compounds were added to adsorbents to analyze the concentration effects.

Fumed alumina (S_{BET} = 89 m^2/g), fumed silica/titania ST (20 wt. % of titania, S_{BET} = 87 m^2/g) and fumed alumina/silica/titania AST (89 wt. % of partially crystalline alumina, 10 wt. % of amorphous silica and 1 wt. % of titania as a small number of titania nanoparticles doped by silica, and alumina and a solid solution of titania in alumina and silica phases, S_{BET} = 83 m^2/g) were used as the initial powder materials (pilot plant of the Chuiko Institute of Surface Chemistry, Kalush, Ukraine). Binary and ternary fumed oxides were prepared by simultaneous high-temperature hydrolysis of the corresponding chlorides ($SiCl_4$, $AlCl_3$, $TiCl_4$). The initial nanooxide materials were described in details elsewhere [7–18]. Notice that four materials from five ones (used as cryonanooxide precursors) having close S_{BET} values (83–89 m^2/g) were selected for more clear analysis of the effects of the chemical composition of nanooxides on the cryogelation results. Two fumed silicas PS300 and PS100 were selected to analyze the influence of the specific surface area on the characteristics of the cryogels.

Aqueous suspensions of nanooxides (20 wt. %) were prepared using doubly distilled water or 0.1 M NaCl solution sonicated (22 kHz) for 5 min. The dispersions were then frozen at 260 K (for 12 or 24 h) or 208 K (for 12 h) in thick-walled stainless steel reactors at pressures of up to 1050 atm, caused by ice crystallites formed in the frozen suspensions (~10–15 mL) placed in strongly restricted volume of the cryo-bombs. The pressure of ice in the cryo-bombs was very high (~1000 atm) [17, 18]. Then cryonanooxide (CNO) samples were dried in glass dishes in air at room temperature for 2–5 days to air-dry state. The same suspensions prepared at standard conditions were kept at room temperature for 24 h and 1 atm to prepare gelled samples and then dried for 2–5 days to air-dry state. All the final materials studied were prepared in the powder state.

^{1}H NMR spectroscopy. ^{1}H NMR spectra of static samples (*i.e.* non-MAS) were recorded at 200–300 K using a Varian 400 Mercury spectrometer (magnetic field of 9.4 T) of high resolution with probing 90° pulses with duration of 3 μs with eight scans and 2 s delay between them. The absence of significant changes in signal intensity of liquid PDMS at T > 245 K (*i.e.* without phase transition) allows one to assume that the spin

system can completely relax between the pulses. Relative mean errors were smaller than ±10 % for ^{1}H NMR signal intensity for overlapped signals and ±5 % for single signals, and ±1 K for temperature. Repeated measurements of PDMS/silica gel and PDMS/nanosilica samples give a similar spectral picture at the same temperature. The ^{1}H NMR spectra were recorded during cooling of samples from 280–290 K to 200–210 K and then during heating to 290–300 at a step ΔT = 10 K and a heating rate of 5 K/min for 2 min and maintained at a fixed temperature for 7 min. In contrast to magic-angle spinning (MAS, including cross polarization MAS, 2D, *etc.*) NMR spectra, here ^{1}H NMR signal intensity was determined for static samples (non-MAS) that allows to control only mobile molecules (liquid PDMS). This is due to short transverse relaxation time of solids (*e.g.* OH groups of silicas) and frozen adsorbates, *i.e.* frozen Oxane 1000 (melting temperature $T_m \approx 231$ K), and the use of a relatively narrow bandwidth of the spectrometer (20 kHz) [7]. This approach can be effectively used in NMR cryoporometry [7]. To determine chemical shift of the proton resonance (δ_H), tetramethylsilane (TMS) was used as an internal standard (δ_H errors < ±0.25 ppm).

Differential Scanning Calorimetry (DSC). The thermal properties of the PDMS/silica samples were investigated in a nitrogen atmosphere at temperatures from 293 to 153 K (cooling) and then to 393 K (heating) using a Perkin Elmer Pyris 6 DSC instrument. The instrument was calibrated using indium sample. Samples of ~8 mg in mass were closed in standard aluminum pans. Cooling and heating rates were the same 10 K/min. During the first scan, the samples were cooled from room temperature (293 K) to 153 K, held for 4 min (isothermally), heated to 393 K and held for 2 min (isothermally) in order to evaporate the contained water. Then during the second scan, the samples were cooled from 393 to 153 K and heated again to 393 K.

Textural characteristics. The textural characteristics of silicas were determined from low-temperature (77.4 K) nitrogen adsorption–desorption isotherms recorded using a Micromeritics ASAP 2405N or 2420 adsorption analyzer or a Quantachrome Autosorb adsorption analyzer. The specific surface area (S_{BET}) was calculated according to the standard BET method [19]. The total pore volume (V_p) was evaluated from the nitrogen adsorption at p/p_0 = 0.98–0.99 (p and p_0 denote the equilibrium and saturation pressure of nitrogen at 77.4 K, respectively).

The nitrogen desorption data were used to compute the pore size distributions (PSDs, differential $f_V(R) \sim dV_p/dR$ and $f_S(R) \sim dS/dR$) using a self-consistent regularization (SCR) procedure [20] under non-negativity condition ($f_V(R) \geq 0$ at any pore radius R) at a fixed regularization parameter $\alpha = 0.01$ [21] with a complex pore model including slit-shaped and cylindrical pores and voids between spherical nonporous nanoparticles packed in random aggregates [20] (the SCV model was used with modified Nguyen-Do (MND) method) [22, 23] for nanosilica and a model of cylindrical pores for silica gel. The differential PSDs (with respect to pore volume $f_V(R) \sim dV/dR$, $\int f_V(R)dR \sim V_p$) were recalculated as incremental PSD (IPSD, $\sum\Phi_{V,i}(R) = V_p$). The differential $f_S(R)$ functions were used to estimate the deviation (Δw) of the pore shape from the model [24]. The $f_V(R)$ and $f_S(R)$ functions were also used to calculate contributions of nanopores (V_{nano} and S_{nano} at 0.35 nm < $R \leq$ 1 nm), mesopores (V_{meso} and S_{meso} at 1 nm < $R \leq$ 25 nm), and macropores (V_{macro} and S_{macro} at 25 nm < R < 100 nm) to the total pore volume and surface area. Additionally, nonlocal density functional theory (NLDFT, Quantachrome software, a model of cylindrical pores) method was used to calculate differential PSDs converted into IPSDs.

HRTEM. High resolution transmission electron microscopy, HRTEM (JEM–2100F, Japan) images were recorded for initial PS300, cryosilica cPS300, initial AST, and cryonanooxides cAST and csAST as representative samples. A powder sample was added to acetone (for chromatography) and sonicated. Then a drop of the suspension was deposited onto a copper grid with a thin carbon film. After acetone evaporation, sample particles remained on the film were studied with HRTEM.

Quantum chemical calculations. Quantum chemical calculations were carried out with *ab initio* and DFT (B3LYP and wB97XD) methods with the 6–31G(d,p) basis set using the Gaussian 09 [25] program suit to full geometry optimization. The gauge-independent atomic orbital (GIAO) method [25] with the DFT method (B3LYP) and the 6–31G(d,p) basis set was applied. Silica clusters modeling a porous silica particle (~1 nm in radius, 1624 atoms) with PDMS (18 units) and

water molecules or decane adsorbed in pore or at the outer surface were calculated by the PM7 method (MOPAC 2012 package) [26, 27]. To calculate the $f(\delta_H)$ functions using the PM7 results, the calibration functions were used to describe the dependence between atomic q_H charges (PM7) and the δ_H values (GIAO/B3LYP/6–31G(d,p)) calculated for small water clusters with 8–64 molecules or small systems with organics or PDMS fragments. To analyze interaction features between PDMS molecules the interaction energy decomposition was carried out follow the Morokuma method with basis set superposition error (BSSE) correction (HF/6–31G(d,p), Firefly 8.1 [28]). The interaction energy was also calculated using the wB97XD functional (appropriate to calculate dispersion interactions) with the 6–31G(d,p) basis set.

RESULTS AND DISCUSSION

Characterization of oxide adsorbents. Initial fumed silica and silica gel (Table 1), initial fumed oxides and cryonanooxides (CNO) (Table 2) are rather mesoporous adsorbents, since contributions of S_{meso} and V_{meso} into S_{BET} and V_p, respectively, are predominant. However, the PSD of silica gels and fumed oxides are very different (Figs. 1 and 2) because of the difference in the porosity type of these materials. The porosity of fumed oxides is due to the textural porosity of the powders as voids between nonporous primary particles forming aggregates and agglomerates of aggregates (Fig. 3) with one exception of AST having more complex structure including both typical nanoparticles of fumed oxides and larger core-shell particles.

Three silica gels studied are characterized by decreased S_{BET} value (Table 1) with increasing average pore radius (R_{av}) and pore volume (V_p). The silica gels are mesoporous (Table 1, S_{meso}, V_{meso}, Fig. 1 *b*) materials, since contributions of nanopores (S_{nano}, V_{nano}) and macropores (S_{macro}, V_{macro}) are much lower than that of mesopores. Pore size distributions (PSD) of silica gels are relatively narrow in contrast to that of nanosilica (Fig. 1). Nanosilica PS400 (as well as other nanooxides) is characterized by the textural porosity corresponding to voids between nonporous nanoparticles (6.7 nm in average diameter) in their aggregates (< 1 μm in size) and agglomerates of aggregates (> 1 μm).

Table 1. Textural characteristics of silicas calculated with models: SCV/SCR for PS400 and the MND method with the model of cylindrical pores for silica gels

Silica	S_{BET}, m^2/g	S_{nano}, m^2/g	S_{meso}, m^2/g	S_{macro}, m^2/g	V_p, cm^3/g	V_{nano}, cm^3/g	V_{meso}, cm^3/g	V_{macro}, cm^3/g	R_{av}, nm	Δw
PS400	409	64	327	18	0.859	0.033	0.550	0.276	4.20	0.388
Si–40	742	188	433	1	0.636	0.077	0.493	0.066	1.71	–0.096
Si–60	456	0	456	0	0.822	0	0.818	0.004	3.61	0.168
Si–100	349	0.3	348	1	1.225	0	1.201	0.024	7.02	0.185

Notice that not all fumed oxides are characterized by the typical particulate morphology with nonporous primary nanoparticles forming loose aggregates. However, the AST sample has more complex structure, since besides typical structures, there core-shell particles with the cores consisting of nanoparticles (mainly alumina nanocrystallites) covered by a shell (Fig. 3). These core-shell structures were partially decomposed during high-pressure cryogelation (HPCG) [18]. Clear, the morphological features of oxide adsorbents can strongly influence the interfacial behavior of adsorbates [7–18]. Nanosilica PS400 is composed of small nanoparticles, which are strongly aggregated, since the bulk density of 0.07 g/cm^3 is slightly larger than the typical values (0.04–0.06 g/cm^3) for a set of nanosilicas at $S_{BET} > 200\ m^2/g$ [7]. Despite predominant contributions of mesopores to the pore volume (Table 1, V_{meso}, V_p) and the specific surface area (S_{BET}, S_{meso}) for PS400, the PSD is very broad because secondary particles of PS400 have a random organization. The deviation of the SCV model from real pores is relatively large for PS400 (Table 1, Δw). It is much greater than that for the cylindrical pore model used for silica gels. In other words, pores in silica gels are more ordered than those in PS400. These textural features of the silicas studied can strongly affect the interfacial behavior of adsorbates, despite the same nature of the pore walls of silicas composed of siloxane bonds ≡Si–O–Si≡ and single silanols ≡SiOH or twin silanols $=Si(OH)_2$ (of a smaller content).

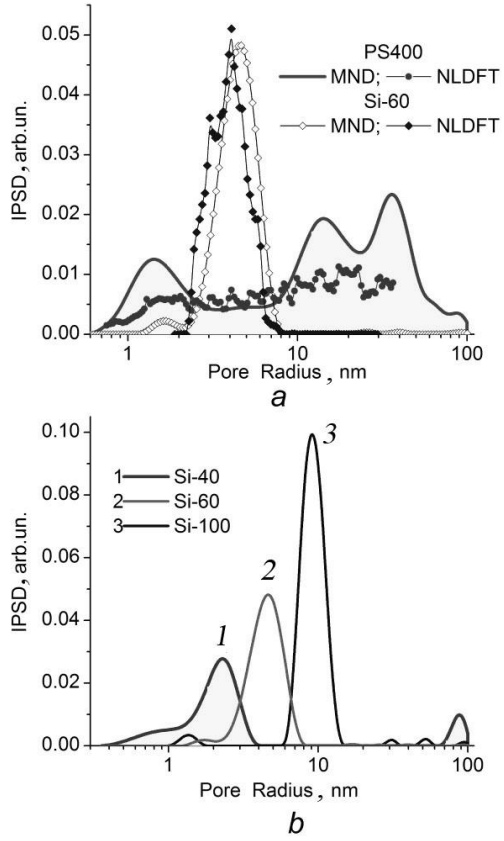

Fig. 1. Incremental pore size distributions: (*a*) SCV/SCR (for PS400) MND and NLDFT for nanosilica PS400 and silica gel Si–60, and (*b*) silica gels (MND with the model of cylindrical pores)

The morphological and textural characteristics are of importance for applications of nanooxides; therefore, changes in these characteristics of CNO are analyzed here in detail (Table 2, and Figs. 2 and 3). Maximal change (double increase) in the specific surface area of CNO (Table 2, S_{BET}) is observed for cAST in comparison with the initial AST powder. This result can be explained by lower stability of relatively large AST core-shell particles at 50–200 nm in diameter (Fig. 3), which represent polycrystalline particles covered by a shell, in comparison with smaller single alumina crystallites or silica nanoparticles. Ternary AST particles are less uniform than binary ST (with much smaller increase in S_{BET} approximately by 3 %) or pure silica and alumina with decreased S_{BET} for CNO during high-pressure cryogelation at low temperature.

Among primary AST nanoparticles there are near pure alumina, silica, and titania nanoparticles [18]. In the presence of a small amount of NaCl (2.8 wt. % in dried samples due to 0.1 M NaCl in the 20 wt. % suspensions), an increase in the S_{BET} value for csAST (by 64 %) and gsAST (by 45 %) is smaller than that for cAST (by 93 %). Salt crystallites formed in rigid pores can damage the materials that depend on pore sizes, as well as on content of salts and water [18]. However, occurrence of this process during cryogelation of the aqueous suspensions is less probable because oxide nanoparticles are nonporous but pores are the voids between nanoparticles in their "soft" loose aggregates. During drying of samples, salt crystallites can form in these voids; *i.e.* they fill a portion of the volume of textural pores and block a portion of the oxide surface [18]. However, this effect is small since the NaCl amount is only 2.8 wt. % and NaCl crystallites are relatively large [18]. Additionally, salt can increase the amounts of residual liquid water during cryogelation; *i.e.*, this can diminish pressure of ice crystallites onto oxide nanoparticles. Perhaps this effect plays the most important role in diminution of the S_{BET} value for csAST and gsAST in comparison with cAST, and decomposition of complex AST nanoparticles decreases (Table 2, Fig. 3).

For a mechanical mixture with AST and PS300 (1 : 1 w/w), after gelation or HPCG and drying the S_{BET} value decreases for mixtures without (gSAST, cSAST, Table 2, by 23 %) and with addition of NaCl (gsSAST, csSAST, by 19 %) in comparison with a non-treated blend powder having S_{BET} = 192 m^2/g. Thus, small nanoparticles of PS300 ($d_{av} \approx 9$ nm) can play a role of a damper decreasing high pressure effects of ice crystallites on larger AST particles ($d_{av} \approx 30$ nm). A small increase (2–3 %) in the S_{BET} value is observed for binary oxide ST after cryogelation and drying. These results for AST and ST can be due to the difference in the temperature/pressure behavior of silica, alumina and titania during extreme treatment of binary and ternary fumed oxides consisting of complex nanoparticles, since similar effects are absent for treated individual fumed silica and alumina.

The S_{BET} value diminution is greater for cPS300 (by 1.7 %) than that for cPS100 (by 0.7 %). It also decreases for CNO with pure alumina (by ~5 %). Thus, for CNO with complex ternary and binary fumed oxides, an increase in the specific surface area can be observed due to partial decomposition of complex nanoparticles characterized by much greater residual stress than such uniform fumed oxides as amorphous silica and

Table 2. Textural characteristics of initial and differently treated nanooxides

Oxide	Medium	T_t, K	P_t, atm	Note	S_{BET}, m^2/g	S_{nano}, m^2/g	S_{meso}, m^2/g	S_{macro}, m^2/g	V_p, cm^3/g	V_{nano}, cm^3/g	V_{meso}, cm^3/g	V_{macro}, cm^3/g	Δw
PS300	–	–	–	initial powder	302	94	200	9	0.734	0.035	0.523	0.176	0.021
cPS300	water	208	1000	cryogel	297	38	258	2	0.827	0.012	0.798	0.017	0.749
gsPS300	0.1M NaCl	293	1	gel/NaCl	292	27	265	1	0.826	0.009	0.807	0.010	0.741
csPS300	0.1M NaCl	208	1000	cryogel/NaCl	283	16	266	1	1.212	0.007	1.193	0.012	0.281
gsPS300*	0.1M NaCl	293	1	gel/NaCl	264	20	242	2	1.257	0.010	1.207	0.040	0.325
gswPS300*	0.1M NaCl	293	1	gel/NaCl washed	276	24	251	1	1.313	0.012	1.263	0.038	0.331
csPS300*	0.1M NaCl	260	1000	cryogel/NaCl	262	27	234	1	1.194	0.015	1.147	0.032	0.362
cswPS300*	0.1M NaCl	260	1000	cryogel/NaCl washed	279	29	248	1	1.291	0.016	1.244	0.031	0.376
PS100	–	–	–	initial powder	84.4	32	49	3	0.206	0.012	0.124	0.070	0.290
gPS100	water	293	1	gel	83.7	8	53	23	0.427	0.003	0.059	0.365	–0.108
cPS100	water	208	1000	cryogel	83.8	28	43	13	0.474	0.014	0.207	0.253	–0.094
Al_2O_3	–	–	–	initial powder	89	12	75	2	0.167	0.006	0.132	0.029	–0.227
gAl_2O_3	water	293	1	gel	76	13	60	2	0.545	0.007	0.504	0.034	0.450
$gsAl_2O$	0.1M NaCl	293	1	gel/NaCl	72	4	43	26	0.521	0.002	0.150	0.369	0.209
$csAl_2O$	0.1M NaCl	208	1000	cryogel/NaCl	72	7	44	22	0.553	0.004	0.238	0.311	0.437
ST	–	–	–	initial powder	87	27	56	4	0.228	0.012	0.144	0.072	–0.291
gST	water	293	1	gel	90	31	49	11	0.365	0.010	0.161	0.195	–0.168
cST	water	208	1000	cryogel	89	30	49	10	0.366	0.010	0.168	0.188	–0.182
gsST	0.1M NaCl	293	1	gel/NaCl	86	33	39	14	0.415	0.010	0.121	0.284	–0.105
csST	0.1M NaCl	208	1000	cryogel/NaCl	88	30	44	13	0.402	0.009	0.138	0.255	–0.100
AST	–	–	–	initial powder	83	12	68	3	0.217	0.005	0.166	0.047	–0.164
gAST	water	293	1	gel	74	6	46	22	0.532	0.003	0.231	0.298	0.363
cAST	water	208	1000	cryogel	160	15	136	9	0.595	0.008	0.466	0.121	0.125
gsAST	0.1M NaCl	293	1	gel/NaCl	120	7	100	13	0.506	0.004	0.294	0.208	–0.060
csAST	0.1M NaCl	208	1000	cryogel/NaCl	133	9	112	13	0.508	0.005	0.305	0.199	–0.090
PS300+AST(gSAST)	water	293	1	gel	147	57	55	36	1.029	0.017	0.374	0.638	0.042
PS300+AST(cSAST)	water	208	1000	cryogel	147	51	62	34	1.098	0.017	0.542	0.539	0.114
PS300+AST(gsSAST)	0.1M NaCl	293	1	gel/NaCl	155	58	62	35	1.064	0.018	0.454	0.592	0.066
PS300+AST(csSAST)	0.1M NaCl	208	1000	cryogel/NaCl	155	58	66	31	1.142	0.018	0.608	0.515	0.123

Note. Labels in dried samples correspond to cryogel (c), cryogel with NaCl (cs), gelation at room temperature (gel, g) with NaCl (gs) and washed samples gelatinised with NaCl (csw or gsw).*Gelation during 24 h, gelation of all other samples was during 12 h

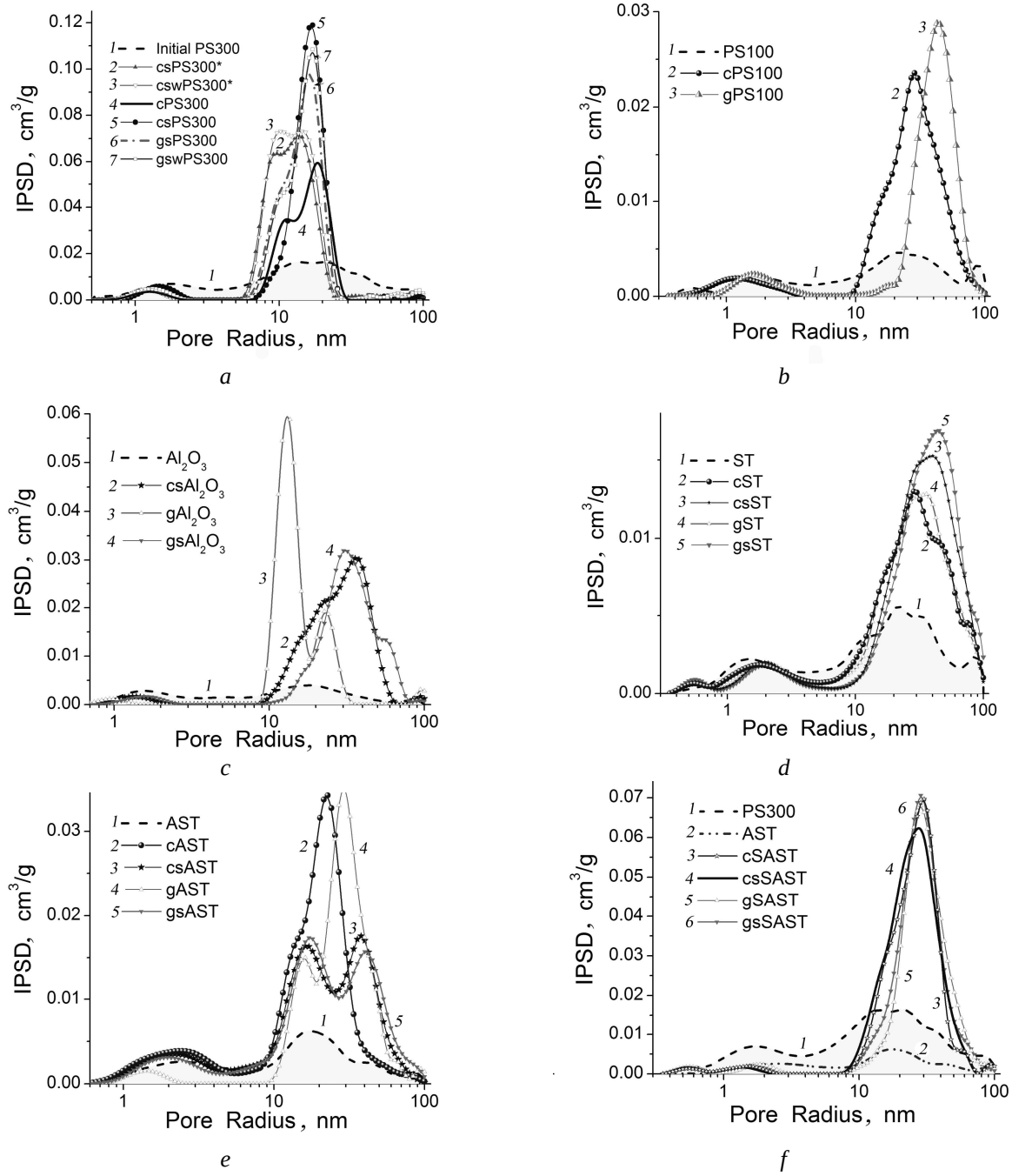

Fig. 2. Incremental SCV/SCR PSD for silicas (*a*) PS300 and (*b*) PS100, (*c*) alumina, (*d*) silica/titania, (*e*) alumina/silica/titania, and (*f*) blend PS300+AST (1:1); initial powder and differently treated nanooxides: cryogelation in pure water at 208 K, in 0.1 M NaCl solution at 260 K or 208 K, suspended in water or 0.1 M NaCl solution and dried at room temperature and standard pressure (sample labels correspond to them in Table 2)

crystalline alumina (mainly with θ-Al_2O_3 which is stable up to 1150 °C and then transforms into α-Al_2O_3). Therefore, the difference in the temperature behavior of silica, alumina and titania phases can lead to cracking of complex nanoparticles during HPCG. For CNO with individual oxides, S_{BET} decreases but nanoparticle sizes do not practically change (Fig. 3) [17, 18] after HPCG and drying. Thus, the S_{BET} value can decrease due to rearrangement (compaction) of aggregates and agglomerates of pure silica or alumina [17, 18].

The pore volume (Table 2, V_p), increases for all the CNO or systems suspended-dried at standard conditions. This is due to the

morphological features and related textural characteristics caused by the formation of loose aggregates with nonporous nanoparticles and very loose agglomerates of aggregates in the initial powders of nanooxides strongly changed during HPCG or gelation. For the initial powders, there is a large empty volume $V_{em} = 1/\rho_b - 1/\rho_0 = 10–25$ cm^3/g, where ρ_b and ρ_0 are the bulk and true density of the materials, respectively. Compaction of nanoparticles in aggregates during HPCG (or even gelation at standard conditions) and drying leads to the opposite effects for V_{em} (which strongly decreases) and V_p (which increases, Table 2). For instance, the gelation/drying leads to an increase in the ρ_b value from 0.067 (PS300) to 0.31 g/cm^3 (cPS300). Therefore, V_{em} decreases from 14.5 (PS300) to 2.8 cm^3/g (cPS300) due to diminution of the volume of macropores, which, however, are poorly filled by such low-molecular weight adsorbates as nitrogen, water, *etc.*, and, therefore, $V_{em} >> V_{macro}$. However, after HPCG or gelation (and compaction of aggregates) despite a decrease in V_{macro}, the V_p value increases due to a significant increase in V_{meso} (Table 2). Similar effects are observed for other studied nanooxides that are, however, smaller due to their larger nanoparticles, an increase in their bulk density, and a decrease in their pore volumes over the total pore size range (Fig. 2, Table 2).

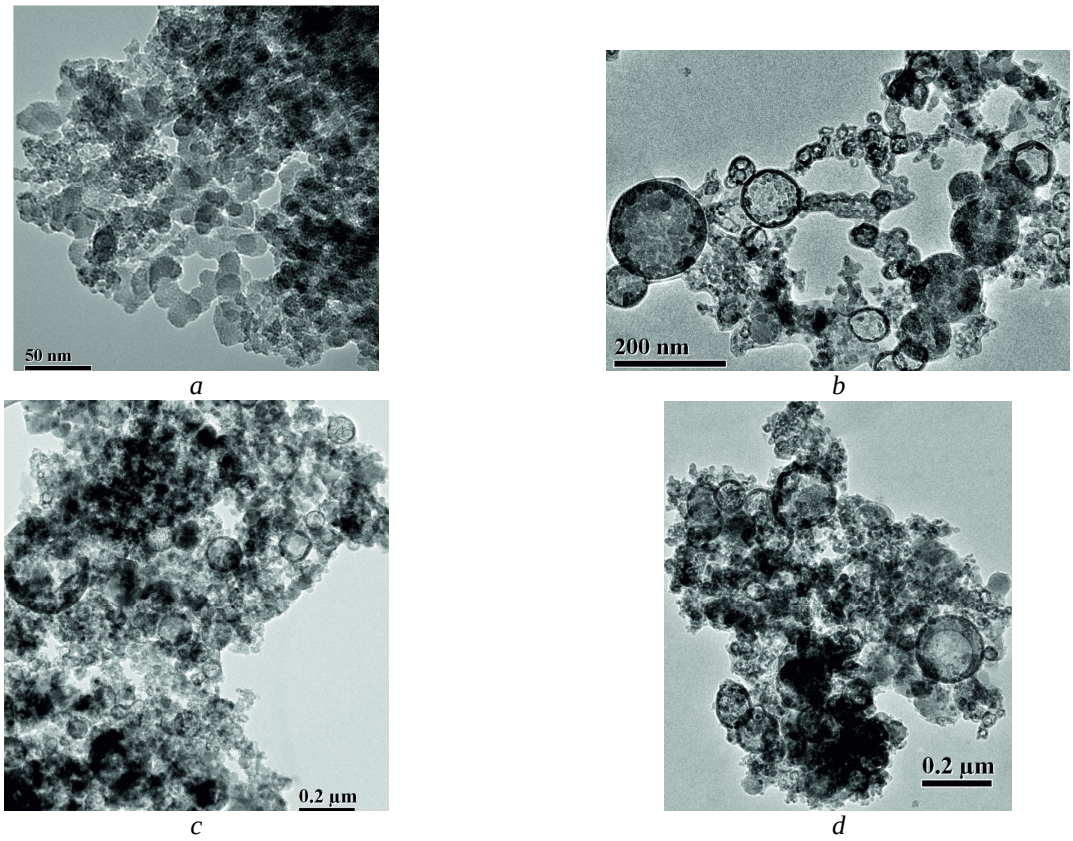

a *b* *c* *d*

Fig. 3. HRTEM images of (*a*) cryogel with cryonanosilica cPS300; (*b*) initial $Al_2O_3/SiO_2/TiO_2$ (AST), (*c*) cryogel with cAST, and (*d*) csAST cryogel with NaCl

According to HRTEM images (Fig. 3), during HPCG and drying of cPS300, the nanoparticle morphology of nanosilica does not practically change [17, 18]. However, the textural characteristics (Table 2, Fig. 2) can significantly change because of rearrangement of CNO nanoparticles in their aggregates and agglomerates. Contribution of nanopores at $R < 1$ nm and narrow mesopores at 1 nm < R < 5–10 nm into the PSD decreases after gelation/drying due to compaction of the aggregates/agglomerates of nanoparticles. In other words, each nanoparticle can be closer to neighboring nanoparticles in CNO than in the initial powder (Fig. 2).

Contribution of large mesopores at 5–10 nm < R < 25 nm and narrow macropores at 25 nm < R <

60–100 nm into the PSD strongly increases after gelation/drying (Fig. 2). However, contribution of large macropores $R > 100$ nm decreases due to compaction of nanooxides after gelation/drying since the bulk density increases by several times. Notice that primary nanoparticles of PS300 have non-ideal spherical shape. Therefore, the SCV/SCR model errors can be relatively large (Table 2, Δw) and the Δw value can increase for CNO because of certain deformation of nanoparticles and changes in the shape of the contact zones between them in aggregates. Therefore, $\Delta w = 0.021$ for the initial PS300 (*i.e.* about 2 % error in the SCV/SCR model) but it increases for cryogels and suspended/dried samples (Table 2, Δw). For PS100, Δw is greater (0.29) than for PS300 (0.02) since the deviation in the particle shape from the spherical one grows with increasing size of primary particles of fumed oxides [7–18].

Interfacial phenomena. The textural features of PS400 results in the formation of relatively large domains of adsorbed water even at a low hydration degree ($h = 0.02$ g/g). This water can be assigned to strongly associated water (SAW) characterized by the chemical shift (δ_H) of approximately 5 ppm (Fig. 4 *a*) close to that of bulk liquid water. In SAW, the average number of the hydrogen bonds per a molecule is 3.5–4.0 that causes $\delta_H \approx 5$ ppm.

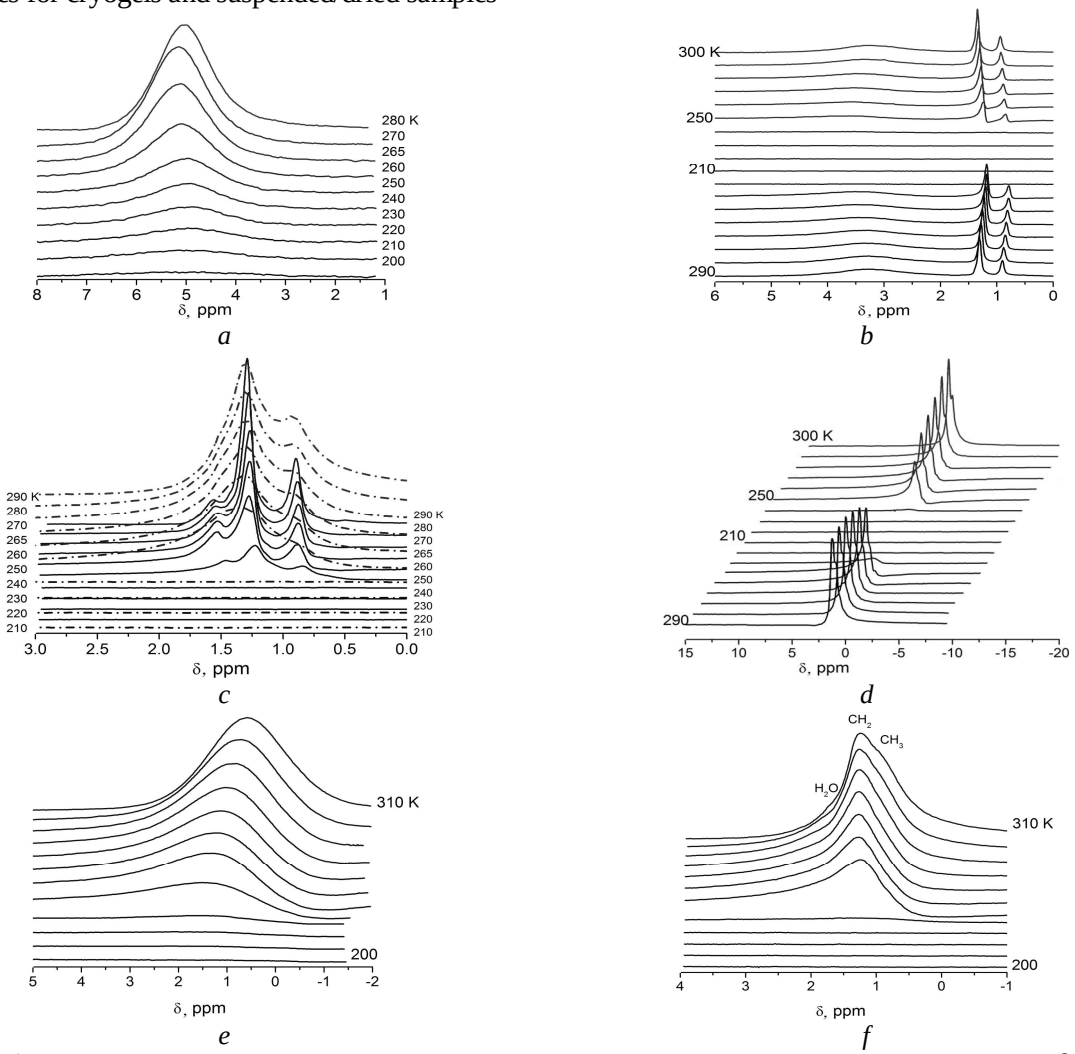

Fig. 4. ^{1}H NMR spectra (for static samples) of adsorbates bound to nanosilica PS400 (*a*-*d*) initial ($\rho_b = 0.07$ g/cm^3) and (*e*, *f*) compacted ($\rho_b = 0.15$ g/cm^3): (*a*) water ($h = 0.02$ g per gram of dry PS400); and water ($h = 0.05$ g/g) and *n*-decane of content C_d = (*b*) 1.5 and (*c*, *d*) 7.3 g/g, (d) with addition of polyphosphoric acid (PPA) at $C_{PPA} = 0.05$ g/g, (*e*) 0.73 and (*f*) 3.7 g/g; (*c*) PS400 initial (solid lines) and heated (dot-dashed lines) at 723 K for 10 min, loaded into the ampoule, heated at 473 K, slightly cooled, decane (7.3 g/g) was added to hot silica and boiled for 1 min

Notice that in liquid water, a portion of molecules is interstitial; *i.e.* they are out of the hydrogen bond network [7]. Therefore, the average coordination number of a water molecule can be about 4.5 (*i.e.* larger than that in ice having, therefore, a lower density than liquid water) but $\delta_{H,lw} < \delta_{H,ice}$ due to thermal distortion of the hydrogen bonds (length O–H···O and angle ∠OHO are non-optimal) and the presence of interstitial water molecules [7]. A fraction of water is unfrozen at $T < 260$ K that corresponds to strongly bound water (SBW) since changes in the Gibbs free energy $\Delta G < -0.5$ kJ/mol [7]. The δ_H value (*i.e.* magnetic shielding of protons) of water depends on the average number of the hydrogen bonds per a molecule ($<n_{HB}>$) and the length O–H···O and angle ∠OHO of these bonds [7]. It is equal to 7.4 ppm for single ice Ih crystals and *ca.* 1 ppm for free water molecules.

Despite water and decane are immiscible liquids, addition of decane (C_d = 1.5 g/g) to silica weakly hydrated (h = 0.05 g/g) results in the upfield shift of ^{1}H NMR signal of water, since the δ_H value changes in the 3.2–3.5 ppm range (Fig. 4 *b*) instead of 4.5–5.0 ppm for water adsorbed alone (Fig. 4 *b*) with a weak dependence of the δ_H value on temperature. This decrease in the δ_H value can be explained by enhanced clusterization of bound water under action of hydrophobic decane. Decane can displace water into both narrower pores (inaccessible for larger decane molecules) and larger pores (to decrease contact area between two immiscible liquids). Both displacements result in decrease in the Gibbs free energy of the system. However, the second type of the displacements is more characteristic for the systems with greater amounts of water than h = 0.05 g/g used here [7]. Despite a relatively great amount of decane (1.5 g/g), the sample remains in the powder state; *i.e.* all decane is in bound state.

The ^{1}H NMR spectra (Fig. 4 *b*, *d*) were recorded for both decreasing (from 290 to 210 K) and increasing (from 210 to 300–310 K) temperatures. Adsorbed decane demonstrates signals at 0.9 and 1.25 ppm (Fig. 4 *b*), corresponding to methyl and methylene groups, respectively. A small shift of decane signals with temperature can be due to the temperature dependence of the magnetic susceptibility of samples and/or changes in the parameters of a resonant circuit of a sensor without stabilization of resonance conditions by using deuterons. During cooling of a sample, signal intensity of both water and *n*-decane strongly decreases at T = 220 K (Fig. 4 *b*). During heating, intensive signals of *n*-decane (and water) appear at $T > T_f$.

A sample placed in the *n*-decane dispersion medium (C_d = 7.3 g/g), stirred at 293 K, is characterized by an additional upfield shift of bound water signal to approximately 1.5 ppm (Fig. 4 *c*), *i.e.* the water clusterization increases in comparison with the sample at C_d = 1.5 g/g (Fig. 4 *b*). Water with similar low δ_H values can be assigned to weakly associated water which represents individual molecules, 1D or strongly branched 2D or 3D clusters at the boundaries of polar (*e.g.* silica) and nonpolar (*e.g. n*-decane) media or mosaic polar-nonpolar structures of the solid surface [7]. The δ_H values for H atoms in the OH groups participating and non-participating in the hydrogen bonds as a proton-donor strongly differ because O atoms or other electron-acceptor atoms displace the electronic density from the H atoms that leads to a decrease in the magnetic shielding of the protons. Therefore, WAW is characterized by a low (≤ 1) average number of the hydrogen bonds per a molecule as a proton-donor. However, this WAW bound to silica corresponds to strongly bound water since its signal appears at $T > 240$ K (*i.e.* $\Delta G < -1$ kJ/mol) when decane signal appears too. This may suggest that water (*i.e.* SBW) locates in narrow voids (pores) corresponding to the first peak of PSD of PS400 at R = 0.6–1.5 nm (Fig. 1).

To analyze the influence of bound water on the behavior of bound *n*-decane, polyphosphoric acid (PPA) was added as a dehydrating agent in the amount corresponding to the amount of water (Fig. 4 *d*). Really, water signal is not observed after addition of PPA, *i.e.* all water is bound to PPA. Signal of water/PPA could be observed at ca. 10 ppm as a very broad signal. Here this signal is not observed (Fig. 4 *d*) due to features of the used measurement technique and a narrow bandwidth (20 kHz) of the spectrometer. The PPA addition leads to a decrease in splitting of decane signals (compare the spectra in Figs. 4 *b*, *c* and 4 *d*). Thus, strong bonding of water by PPA leads to enhancement of interaction of bound decane with the silica surface.

Pretreatment of PS400 (heating at 723 K for 10 min, loading a hot sample into a NMR ampoule, heating at 473 K, slight cooling, and then addition

of decane to hot silica sample and boiling in decane for 1 min) was used to reduce the silica surface hydrophilicity. This treatment results in diminution of decane melting delay (Figs. 4 *c* and 5) since signal intensity of a fraction of mobile decane increases much stronger at $T > T_f$, especially at $T > 260$ K. This result can be explained by a better distribution of silica nanoparticles (in comparison with the initial silica) in the decane medium and stronger interaction of decane with the silica surface, which is characterized by a decreased number of surface silanols and lower amount of residual water due to heating under the mentioned conditions. The stronger interaction of decane with the silica surface appears in broadening of the ^{1}H NMR bands (Fig. 4 *c*, dot-dashed lines) similar to samples at a low content of decane located only in pores of silica.

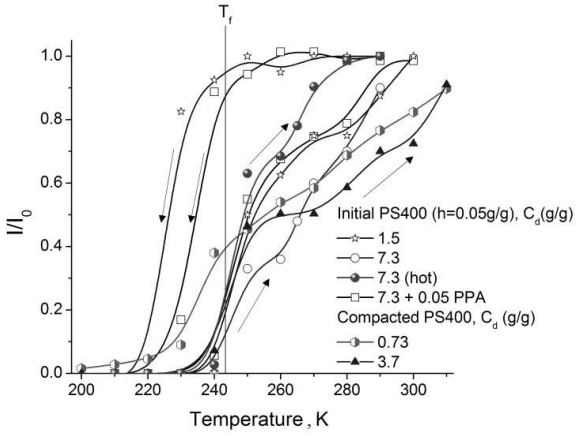

Fig. 5. Temperature behavior of signal intensity (normalized to intensity I_0 at 290–310 K) of *n*-decane bound to initial (bulk density 0.07 g/cm^3) and compacted (0.15 g/cm^3) PS400 depending on C_d and presence of PPA; curve labeled as 'hot' corresponds to PS400 heated at 723 K for 10 min, loaded into the ampoule, heated at 473 K, slightly cooled, and addition of decane to hot silica and boiling in decane for 1 min

Freezing/melting curves, shown as relative intensity of ^{1}H NMR signals of mobile decane molecules confined in textural pores of PS400, are characterized by a broad hysteresis loop (Fig. 5). This is due to melting of solid alkane structures with a certain delay in comparison with their freezing at the same temperatures. During heating of the frozen PS400/water/decane system at $C_d = 7.3$ g/g, melting of a significant fraction of decane occurs at temperatures higher than the freezing point ($T_f = 243.5$ K) of bulk decane (Fig. 5). An increase in signal intensity is observed up to 280–310 K. Addition of PPA leads to certain changes in the freezing and melting temperatures of decane. During freezing, a strong decrease in the signal intensity of decane is observed at 220–230 K, *i.e.* at $T < T_f$ (Fig. 5). This effect can be due to relatively weak interaction of a significant fraction of decane (frozen at $T > 230$ K) with the pore walls. This is clearly seen from the difference in the freezing curves at different content of decane. Since at $C_d = 7.3$ g/g (only ~20 % decane is unfrozen at 230 K) a fraction of decane weakly bound or non-interacting with the silica surface is much greater than that at $C_d = 1.5$ g/g (~80 % decane is unfrozen at 230 K) because decane located in pores is unfrozen at 230 K due to freezing point depression under the confined space effects.

Samples of silica gel Si–60 were prepared with different amounts of *n*-decane ($C_d = 0.44$ and 3.7 g/g). Si–60 was heated at 445 K, and then decane added to cooled silica filled a portion of pores ($C_d = 0.44$ g/g) or completely filled of pores and formed the dispersion medium ($C_d = 3.7$ g/g). The last Si–60/alkane sample was heated at 445 K for 1 min to remove air bubbles from pores, and it was transparent after this heating; *i.e.* pores are filled by liquid. It included *ca.* 0.005 g/g of residual water (Fig. 6 *a*). The decane amount of 0.44 g/g (liquid density of decane is 0.73 g/ml) provides filling of a major portion (0.6 cm^3/g) of pores of Si–60 (Table 1, V_p). At decane excess, the ^{1}H NMR spectra include two relatively broad signals at 1.25 and 0.9 ppm at $T > T_f \approx 243$ K (Fig. 6 *a*). Signal of residual water appears as a shoulder at 1.5 ppm. Additionally, methylene groups linked to CH_3 groups in the decane molecule can contribute this signal at 1.5 ppm. Water bound in this sample corresponds to WAW, as well as in the case of alkane/PS400 system (Fig. 4).

At $T \leq 240$ K, the signal width decreases and the upfield shift is observed due to changes in the magnetic susceptibility of the sample with a frozen fraction of decane. At $C_d = 0.44$ g/g when alkane molecules are located only in pores of Si–60, signals of methyl and methylene groups are broadened, overlapped and characterized by a small downfield shift with decreasing temperature (Fig. 6 *b*). This effect is much stronger than that for decane bound to the treated PS400 sample with a greater content of alkane (Fig. 4 *c*). This difference can be explained by stronger confined space effects

for decane located in narrow mesopores of rigid silica gel beads in comparison with the 'soft' PS400 powder characterized by the textural porosity only.

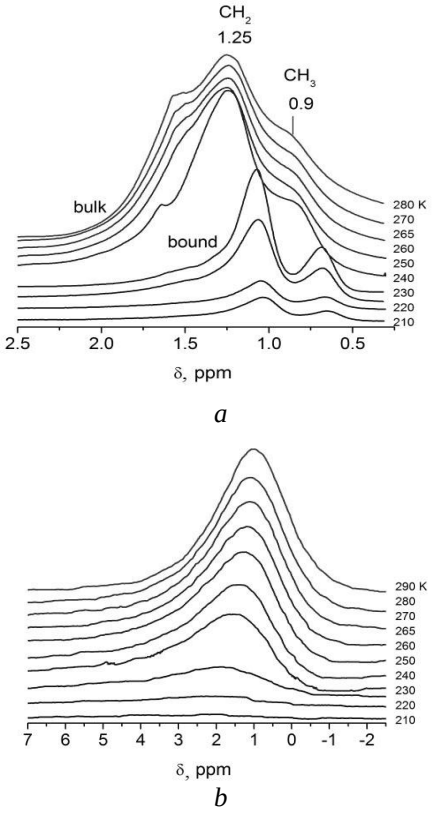

Fig. 6. ^{1}H NMR spectra (for static samples during heating) of adsorbates bound to Si–60 at decane amount C_d = (*a*) 3.7 g/g (total filling of pores by decane) and (*b*) 0.44 g/g (partial filling of pores) and residual water at $h \approx 0.005$ g/g

At $T < T_f$, the temperature dependences of signal intensity of decane are similar for both samples with Si–60 at C_d = 3.7 or 0.44 g/g (Fig. 7) but they are located above that of PS400 at C_d = 7.3 g/g due to a greater excess of bulk decane in the last sample. This causes signal appearance only at $T > 240$ K during thawing of frozen decane/PS400 with significant melting delay (Fig. 7). Consequently, a greater amount of decane bound to Si–60 is unfrozen in comparison with the PS400 sample at the same temperatures. This difference can be explained not only by the difference in the amounts of decane but also by the difference in the texture of these silicas (Fig. 1, Table 1). At C_d = 3.7 g/g, the total amount of alkane is unfrozen at $T > T_f$ during heating (Fig. 7) in contrast to the sample at a low amount of decane (0.44 g/g). This effect is due to a very small outer surface area of Si–60 beads which could weakly affect the temperature behavior of decane located out of pores.

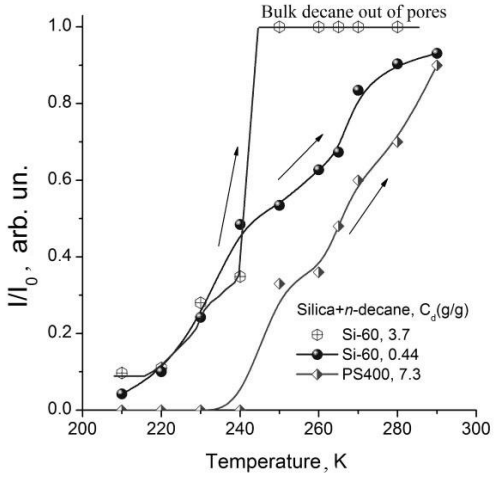

Fig. 7. Temperature behavior of signal intensity (normalized by dividing by the intensity I_0 at maximal temperature used, 290–300 K) of decane bound to Si–60 at C_d = 3.7 and 0.44 g/g or PS400 at C_d = 7.3 g/g during heating regime

Therefore, the effect of the silica gel on bulk alkane (melting delay) out of pores is much smaller than that for nanosilica having a much greater outer surface of aggregates of nanoparticles which affect a greater amount of nearly bulk decane and enhances the melting delay. Notice that similar structurization effects were observed for aqueous suspensions of nanosilicas since 10–12 wt. % of nanosilica was enough for total structurization of all water in the suspension [7]. If entire decane is bound in pores of Si–60 at C_d = 0.44 g/g, its fraction is immobilized at $T > T_f$, and an intensity increase is observed up to 280–310 K similar to that for decane/PS400 (Figs. 5 and 7); *i.e.* solid or quasi-solid decane structures do not melt due to the effect of silicas and this effect is stronger for nanosilica. In other words, the same amount of PS400 can structure a much greater amount of decane (out of pores) than silica gel. Thus, different morphological characteristics of PS400 and Si–60 at close S_{BET} values lead to very different effects on decane located in pores and out of pores.

The $\delta_H(T)$ function depends on the number of possible configurations of the water molecules in the hydrogen bonds network. Considering that this number is inversely proportional to the average number of the hydrogen bonds $<n_{HB}>$ according to the entropy definition $S \approx -k_B \ln n_{HB}$ [13]. Therefore, the temperature derivative of the measured fractional chemical shift

$$-\left(\frac{\partial \ln \delta(T)}{\partial T}\right)_p = -\left(\frac{\partial \ln < n_{HB} >}{\partial T}\right)_p \approx \left(\frac{\partial S}{\partial T}\right)_p \quad (1)$$

should be proportional to the constant pressure specific heat $C_P(T)$ ($C_P = T(\partial S/\partial T)_P$). This aspect is analyzed in detail elsewhere. Here the $T(\partial \ln\delta(T)/\partial T)_P$ functions are compared for water and decane bound to PS400 and Si–60 (Fig. 8).

Heating of Si–60/decane (C_d = 0.44 g/g) frozen at 210 K leads to an increase in the entropy (Fig. 8, curve *1*) at T < 230 K. Then the entropy decreases (minimum is at 243 K ≈ $T_{f,decane}$) due to ordering of mobile molecules at $T < T_{f,decane}$. At $T > T_{f,decane}$, the entropy increases due to increasing disorder in a melt fraction of the adsorbate. The next minimum at *ca.* 273 K (*i.e.* at $T_{f,water}$) is due to the effects of ordering (separating) mobile water and decane (Fig. 7). Excess of decane (C_d = 3.7 g/g), when it plays a role of the dispersion medium for Si–60 beads, results in much lower entropy at $T_{f,decane}$ (Fig. 8, curve *2*) due to freezing of the major portion of decane at $T < T_{f,decane}$ (Fig. 7). In the case of adsorbed water (Fig. 8, curves *3* and *4*), the entropy decreases at T close to $T_{f,water}$ and then it increases due to increasing disorder of liquid water with increasing temperature.

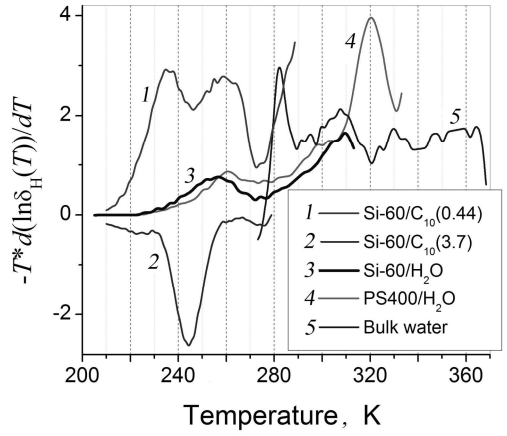

Fig. 8. Function $-T(\partial \ln\delta(T)/\partial T)_P$ *vs.* temperature for *n*-decane (C_{10}) and water (0.05 g/g) bound to Si–60 or PS400 or bulk water

Theoretical calculations of the ^{1}H NMR spectra of *n*-decane and water molecules free and bound in silica mesopore (1.1 nm in radius) or to a silica nanoparticle (~2.1 nm in diameter) show (Fig. 9 *a*) that the interaction with silica results in downfield shift of the band maximum of decane and broadening of the spectrum (Fig. 9 *a*, curves *3* and *4*). This occurs despite weak interactions between a silica surface and nonpolar alkane molecules. The effect is stronger for decane molecules located in the narrow pore (curve *4*) than that for the molecules bound to the silica nanoparticle (curve *3*). Water molecules co-adsorbed with decane without formation of clusters are characterized by a band at 1–2 ppm (Fig. 9 *a*, curve *5*), i.e. this is WAW. These results are in agreement with the experimental data showing the WAW appearing due to co-adsorption with decane (Figs. 4 and 6). Notice that decane-decane interaction is relatively weak. For instance, the free energy of solvation of *n*-decane in the *n*-decane medium calculated using the SMD method (HF/6–31G(d,p) basis set) gives –16 kJ/mol. This is approximately 2.5 times smaller (by the modulus) that the solvation energy of silica in water. Therefore, the spectra calculated for decane molecules free and in the decane dispersion medium are practically the same in contrast to the molecules free and interacting with the silica surface because the interaction of a decane molecule with the silica surface is stronger than that with neighboring decane molecules. Interaction of water molecules with the PPA fragments causes significant downfield shifts for both water molecules (compare curve 1 in Fig. 9 *b* and curve *5* in Fig. 9 *a*, $\Delta\delta_H$ = 3–5 ppm) and OH groups in the PPA (compare curves *2* and *3* in Fig. 9 *b*, $\Delta\delta_H$ = 5–7 ppm). This effect is a typical downfield shift for acids interacting with water molecules due to decreasing of the electron density on the H atoms (*i.e.* decreasing magnetic shielding of protons) which tend to be de-attached as H^+ to form $H_3O^+(H_2O)_n$ (Eigen and Zundel cations) and acidic residua both strongly affecting the water structure. Notice that in the case of the strongest hydrogen bonds of basic compounds with strongly acidic OH groups, the chemical shift of protons can reach much higher values up to δ_H = 16–20 ppm.

The interaction energy of water or decane with silicas, measured as the heat of immersion of powder samples in liquids, increases with increasing specific surface area of silicas (Fig. 10). The curve course is practically the same for nanosilicas and silica gels interacting with water because of the identity of the nature of their surfaces composed of the siloxane bonds and the silanol groups. The latter (in contrast to the siloxane bonds) are the main adsorption sites for water. For the alkane medium, the increase in the interaction energy with increasing S_{BET} is smaller

than that for the aqueous medium. For silica gels, the ratio $K = Q_{water}/Q_{decane}$ is large (2.5–3.3), because silica gels are highly hydrophilic materials, and it grows with S_{BET} value. For nanosilicas, the K values are smaller (1.2–1.5) due to a smaller number of surface silanols (~2 OH/nm^2) than that on the silica gel surface (~5 OH/nm^2).

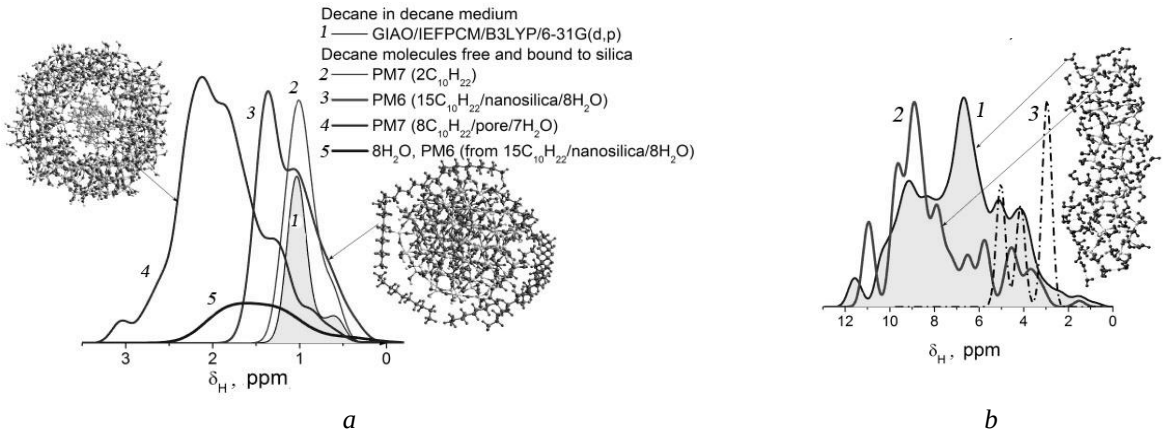

Fig. 9. Theoretically calculated ^{1}H NMR spectra of (*a*) *n*-decane and water molecules free (curves *1* and *2*) and bound in mesopore of silica (curve *4*) or to silica nanoparticle (curves *3, 5*); and (*b*) water (curve *1*, PM7) and OH groups in PPA fragments hydrated (2, PM7) and non-hydrated (3, GIAO/B3LYP/6–31G(d,p))

This difference is a consequence of the flame synthesis of nanosilicas at high temperatures (> 1200 K) in contrast to silica gels synthesized in the liquid reaction media. This leads to greater Q_{decane} values for nanosilicas caused by stronger dispersion interactions with more open surface of nanosilicas than for silica gels with similar S_{BET} values. Thus, nanosilicas are less hydrophilic (it adsorbs only 1–3 wt. % of water from air) than silica gels. Additionally, the surface area of nanosilicas (possessing the textural porosity caused by aggregates < 1 μm in size of nonporous nanoparticles < 10 nm in size) is more accessible for relatively large molecules of *n*-decane (Fig. 9) than that of silica gels representing rigid mesoporous particles of sizes in the millimeter range, *i.e.* possessing narrow and long mesopores. Dispersion interactions of decane molecules with the silica surface are weaker than the hydrogen bonding of water molecules to the surface silanols (per mole of silanols), but are greater per mole of adsorbates due to a much larger size of $C_{10}H_{22}$ than H_2O [7]. Additionally, the narrowest pores of silica gels are less accessible for decane molecules larger by approximately ten times than water molecules. Adsorbed water molecules form clusters around surface hydroxyls that can reduce the effects of different numbers of surface hydroxyls per nm^2 of surface of nanosilicas and silica gels studied. Therefore, the curves of Q_{water} *vs.* S_{BET} (Fig. 10) have similar courses for nanosilicas and silica gels. The difference in the K values for these silicas is mainly due to the difference in the Q_{decane} values. For instance, Q_{decane} = 34.4 and 17.4 J/g for PS300 and Si–100, respectively, with similar S_{BET} values. Stronger interactions of *n*-decane with less hydrophilic nanosilicas than with more hydrophilic silica gels can explain the difference in the temperature behavior of ^{1}H NMR signal intensity of *n*-decane bound to nanosilica PS400 and silica gel Si–60 (Figs. 5 and 7).

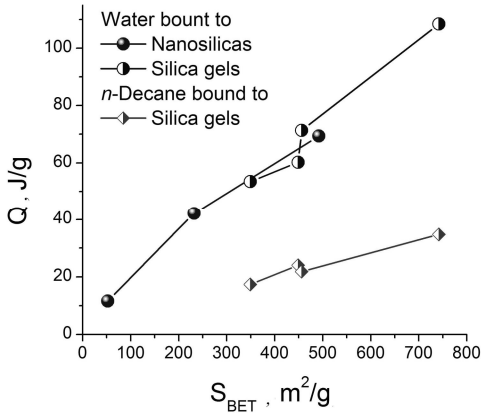

Fig. 10. The relationship between the heat of immersion of nanosilicas and silica gels in water or decane *vs.* the specific surface area (S_{BET}) of silicas

DSC thermograms of cooling of *n*-decane, adsorbed onto different silica gels in the amounts

greater than the pore volume of silicas, demonstrate the presence of two crystallization peaks (Fig. 11). A low-temperature crystallization peak shifts toward higher temperature with increasing pore size (Fig. 11). The shift of a low-temperature melting peak with respect to a low-temperature crystallization peak depends on the pore size distribution of silica gels because melting of larger frozen structures bound in larger pores occurs at higher temperatures (Fig. 11 *b*, *c*) since the heating rate of 5 K/min used is not too small. This causes certain delay in the melting process. Therefore, the hysteresis loop can be broader for decane adsorbed in broader pores due to the formation of larger frozen structures (quasi-crystallites). Similar effects are observed (Figs. 5 and 7) for different amounts of decane adsorbed onto the same silica because it fills only narrower pores at a lower content. A narrow peak at T close to T_f (Fig. 11) is due to freezing of nearly bulk decane weakly bound or unbound to silica gels because decane was adsorbed in the amounts greater than the pore volume. Consequently, there is a fraction of decane weakly bound or unbound to the silica surface. The second peak, which is located at lower temperatures and broader than the first one but it depends on the pore size of silica gels, appears due to freezing of decane bound in mesopores. Melting curves of decane at $T < T_{f,d}$, *i.e.* for alkane located in pores, and water crystallites at $T < T_{f,w}$ confined in narrow pores of Si–40 are similar in shape as they demonstrate broad peaks but different in position (Fig. 11 *a*) because these adsorbates are of very different nature and are characterized by different types of intermolecular bonding affecting T_f. Water does not show the melting peak at $T \geq T_{f,w}$ (Fig. 11 *a*, curve *4*) because entire water (h = 0.35 g/g) is bound in narrow pores of Si–40. During freezing of the sample (Fig. 11 *a*, curve *3*), a narrow crystallization peak is observed at *ca.* 273 K (*i.e.* there is strongly associated but weakly bound water) in addition to a broad crystallization peak at 230–250 K for water strongly bound in pores. During melting of ice bound in pores of Si–40, the heterogeneity of adsorbent and step-by-step melting of ice in broader pores result in the absence of a sharp melting endotherm at temperatures close to $T_{f,w}$ (Fig. 11 *a*, curve *4*). Residual water bound to Si–60 gives a small crystallization peak at 256 K (Fig. 11 *b*, curve *1*).

1-Decanol ($T_{f,dl}$ = 279.5 K, less polar than water but more polar than decane) bound to Si–60 or Si–100 (Fig. 11 *b*, *c*) demonstrates two freezing peaks and two melting peaks. Despite a relatively low amount of decanol bound to Si–60 (0.45 g/g), a sharp freezing exotherm is observed close to its freezing point $T_{f,dl}$ (Fig. 11 *b*). Decanol bound to Si–100 (C_{dl} = 1.11 g/g) demonstrates broader peaks than that bound to Si–60. This difference is similar to that for decane adsorbed onto these silicas.

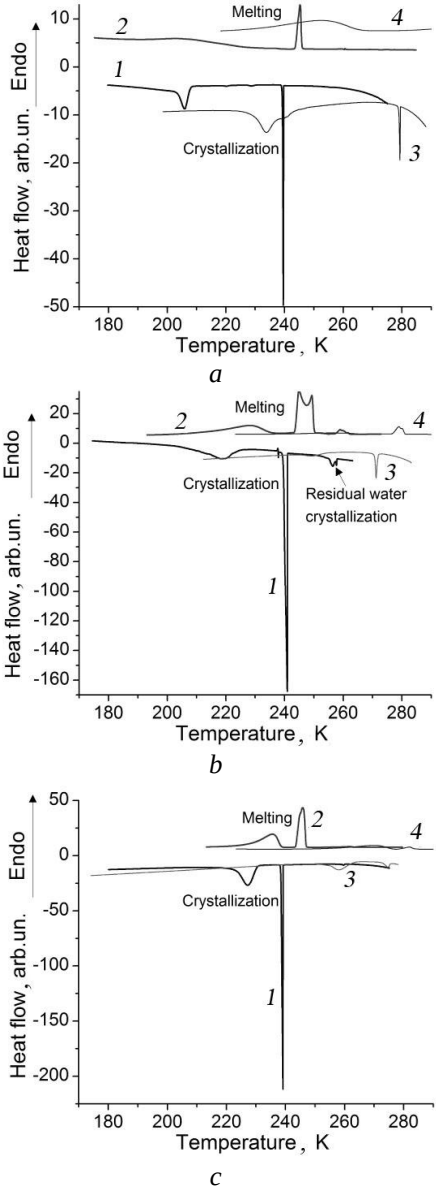

Fig. 11. DSC thermograms of cooling-heating of (*a*-*c*) *n*-decane (curves *1* and *2*), water (curves *3* and *4*), and (*b*, *c*) 1-decanol (curves *3* and *4*) bound to silica gels for (*a*) Si–40 (C_d = 0.61 g/g, h = 0.35 g/g), (*b*) Si–60 (C_d = 1.15 g/g, 1-decanol C_{dl} = 0.45 g/g), and (*c*) Si–100 (C_d = 1.11 g/g, C_{dl} = 1.11 g/g) at the cooling-heating rate of 5 K/min, silica sample mass was 12.8–25.6 mg

Thus, there are several factors governing the temperature behavior of polar (water), weakly polar (1-decanol), and nonpolar (*n*-decane) compounds bound in pores or located out of pores of different silica gels Si–40, Si–60, and Si–100. The first one is the pore size, since the temperature changes in the structure of bound liquids are more homogeneous for adsorbates located in narrower pores with a narrow PSD. The second one is the amount of adsorbate, which can be strongly or weakly bound to the surface of adsorbent or unbound (bulk), located out of pores. Additionally, the heating-cooling rate and the temperature gradient can affect the interfacial and temperature behavior of adsorbates, especially if adsorbents have broad PSDs that cause the formation of inhomogeneous structures (liquid–solid) of adsorbates at different temperatures in pores of different sizes. The temperature dependence of the behavior of liquids confined in pores is the basis of several porosimetry methods, including DSC thermoporometry.

The Gibbs-Thomson (GT) equation applied to DSC melting thermograms [7] allows us to calculate the PSDs for silica gels (with the model of cylindrical pores since the errors of this model are relatively small for silica gels, Table 1, Δw) using melting curves at $T < T_f$, *i.e.* using the low-temperature DSC peaks. Melting curves of decane at $T < 243$ K (Fig. 11) were used to calculate the PSDs with the equation $R = k_{GT}/(T_{0,m} - T_m)$ for cylindrical pore radius at $k_{GT} = 64.6$ K nm, where $T_{0,m}$ and T_m are the melting temperatures for pure bulk crystallites and confined in pores of radius R, respectively. For the freezing point depression of decane confined in pores, these calculations give the PSDs similar to the NLDFT PSDs (Fig. 12 *a*) as well as in the case of bound water (Fig. 12 *b*). Notice that the DSC PSDs have a simple contour than the NLDFT PSD curves because the latter were calculated using a small value of the regularization parameter fixed in the Quantachrome software. For Si–40, DSC PSD (Fig. 12, curve *1*) is zero at $R = 1.0$–1.5 nm in contrast to NLDFT PSD (curve *2*). This difference can be explained by two factors: (i) decane is poorly adsorbed in narrow pores at $R < 1.5$ nm due to presence of residual water and air bubbles; and (ii) the used temperature was not enough low to describe the adsorption of decane in the narrowest pores (melting curve starts from nonzero values, Fig. 11 *a*, curve *2*). Hence, the appropriate correspondence between the NLDFT and DSC PSDs for silica gels is evidence that the melting low-temperature peaks of decane are due to alkane molecules located in mesopores of silica gels.

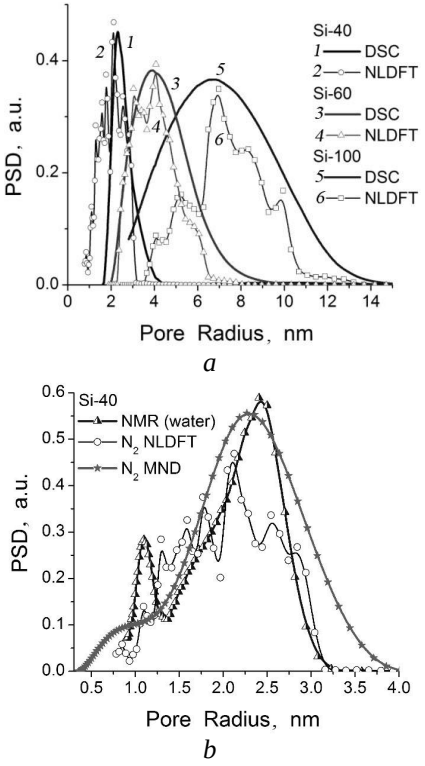

Fig. 12. Differential PSDs of silica gels calculated using (*a, b*) the NLDFT method (applied to nitrogen adsorption-desorption isotherms with the model of cylindrical pores) and the Gibbs–Thomson equation for the freezing point depression for *n*-decane confined in pores using (*a*) DSC melting thermograms, (*b*) the amounts of unfrozen water $C_{uw}(T)$ determined from the ^{1}H NMR spectra of water bound to silica gel Si–40

Maximal excess in the decane amount was for Si–60 ($V_d = 1.58$ cm^3/g at $V_p = 0.82$ cm^3/g). Therefore, a marked high-temperature peak at $T \approx 263$ K is observed for Si–60 (Fig. 11 *b*). However, Si–60 has narrower pores than Si–100 (Fig. 12). Therefore, decane structures confined in mesopores have maximal sizes for Si–100 but the frozen decane structures out of pores can be larger for Si–60. A minimal C_d value (slightly higher than the pore volume) is for Si–40, possessing the narrowest pores (Fig. 12) with the highest adsorption potential [7].

The differences in the PSDs of silicas and the decane excess lead to different hysteresis loops for integrated heat flow ($\Phi(T)$)

$$\Phi(T) = \int_{T_{\min}}^{T} |F(T)|\, dT \qquad (2)$$

during cooling (exo-effects due to crystallization) and heating (endo-effects due to melting) of decane bound to silicas (Fig. 13).

For easier comparison of the $\Phi(T)$ graphs, the integration in Eq. (2) of both freezing and melting curves (after subtraction of a nonlinear baseline) for the modulus of the heat flow $|F(T)|$ was carried out from a minimal temperature (~170 K) toward higher temperatures (~290 K). The $\Phi(T)$ curves for decane bound to Si–60 and Si–100 are similar (Fig. 13 *b, c*) but strongly differ from that for alkane bound to Si–40 (Fig. 13 *a*). This difference can be explained not only by the difference in the PSDs of these silicas (Figs. 1 and 12) but also by the smallest amount (0.61 g/g) of decane adsorbed on Si–40. A nearly vertical step on the $\Phi(T)$ curve of freezing of bulk (or nearly bulk) decane at *ca.* 240–243 K is greater for Si–60 (with maximal excess of adsorbed alkane) than for Si–100 or Si–40 (Fig. 13) due to larger decane structures formed out of pores of Si–60, despite pore sizes of Si–100 are greater than that of Si–60 (Fig. 12). Larger structures of nearly bulk decane give a greater exothermic effect during freezing, as well as a greater endothermic effect during melting (Figs. 11–13). Notice that a certain inclination of a step around T_f is observed on the melting curves, especially for Si–60 and Si–100 (Fig. 13 *b, c*) due to certain delay in melting of large frozen structures during heating at $T > T_f$. These DSC results allow one to explain broad hysteresis loops for the integral ^{1}H NMR intensity for decane, both bulk and confined between silica nanoparticles of A-400 (Fig. 5), as well as for decane bound to Si–60 (Fig. 7) depending on the excess of the alkane. The effect of decane excess in the case of freezing-thawing during ^{1}H NMR measurements can result in the formation of large quasi-solid structures (quasi-crystallites) which are not observed in the ^{1}H NMR spectra recorded at a narrow bandwidth (20 kHz) because of a relatively short time of transverse relaxation of an immovable fraction (despite appearance of a fraction of unfrozen bulk decane at $T > T_f$). In the case of DSC measurements (Fig. 11), a relative significance of this effect is smaller (since only a small peak is at $T \approx 263$ K) due to a smaller decane excess and a certain physical difference in the phenomena studied here by the NMR (changes in the molecular mobility with temperature) and DSC (release or absorption of heat with decreasing or increasing temperature) methods.

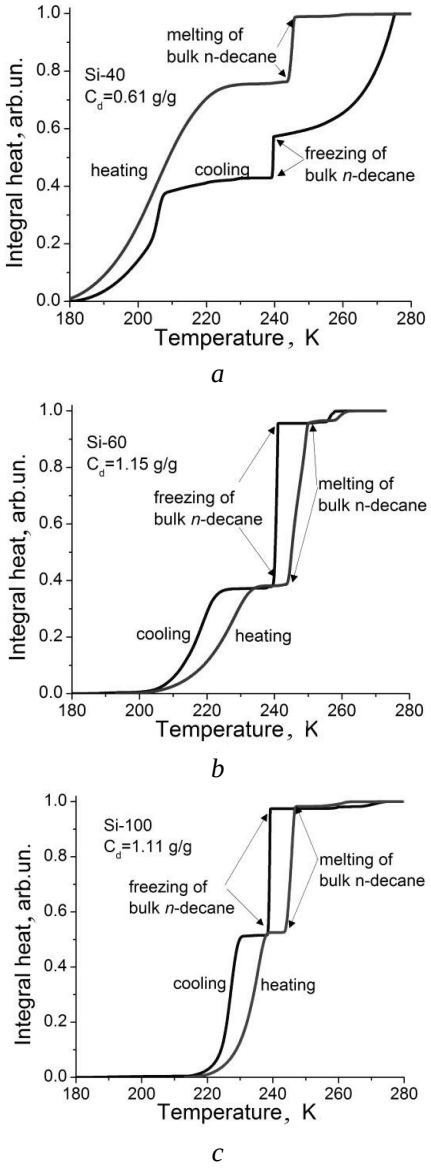

Fig. 13. Integral heat as a function of temperature $\Phi(T)$ (with subtraction of a nonlinear baseline and normalization to unit) for exo (cooling, crystallization) and endo (heating, melting) effects for decane confined in pores of (*a*) Si–40, (*b*) Si–60, and (*c*) Si–100

Significant changes in the texture and structure of cAST in comparison with AST and gAST (Table 2, Figs. 2 and 3) lead to a difference in the interfacial behavior of water alone or in the presence of decane (Figs. 14 and 15). Small amounts of water (0.1 g/g) and decane (0.15 g/g)

were used to fill only a portion of pores of the materials (approximately V_p half of cAST and gAST, Table 2). The greatest difference in the ^{1}H spectra is observed for AST samples with water/decane in chloroform-*d* with addition of trifluoroacetic acid (TFAA) (Fig. 14 *b*). This is due to the influence of the texture of AST (differently changed for gAST and cAST as shown above), *i.e.* confined space effects, on organization of both water and decane and dissolution of TFAA in this water. A maximal amount of TFAA is dissolved in water bound to AST since the ^{1}H NMR peak is at δ_H = 9–10 ppm. The TFAA amounts dissolved in water decrease for gAST and are minimal for cAST. For treated AST (gAST and cAST), decane displaces water into narrower voids (comp. Figs. 15 *a* and 15 *b*). Chloroform medium enhances this trend [18]. A minimal effect of the chloroform medium is for water bound to AST, *i.e.* water structures bound to AST are larger than those bound to gAST or cAST. Therefore, TFAA can be better dissolved in water bound to initial AST.

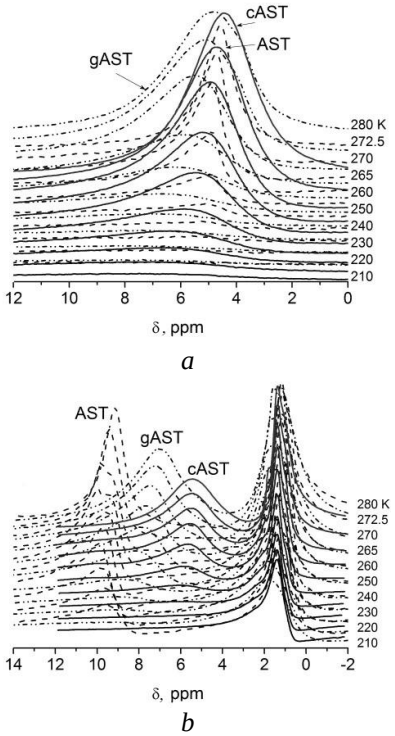

Fig. 14. ^{1}H NMR spectra of (*a*, *b*) water (0.1 g/g) and (*b*) *n*-decane (0.15 g/g) bound to fumed alumina/silica/titania AST (89 wt. % of partially crystalline alumina, 10 wt. % of amorphous silica, and 1 wt. % of titania, S_{BET} = 83 m^2/g) (dashed lines), suspended/dried AST, gAST (dot-dashed lines) and high-pressure cryogel (208 K, 1000 atm) cAST (solid lines) in media (*a*) air and (*b*) $CDCl_3$ with addition of TFAA (6 : 1)

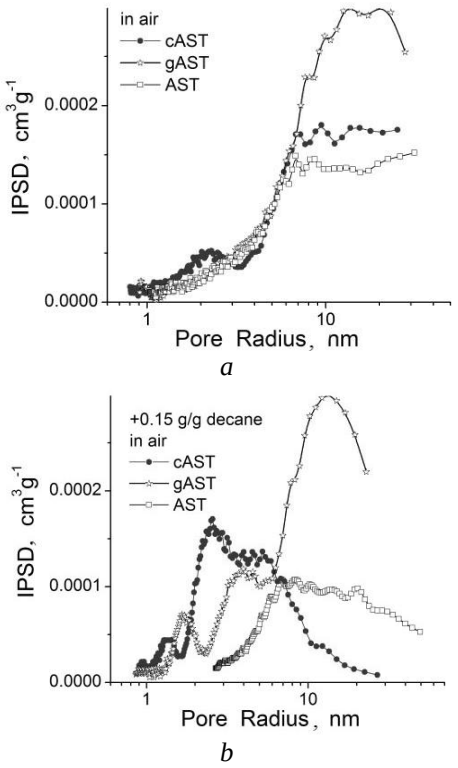

Fig. 15. Incremental PSD calculated from ^{1}H NMR spectra of (*a*, *b*) water (0.1 g/g) bound to AST, gAST and cAST (*b*) with addition of *n*-decane in air

Weakly associated water characterised by δ_H = 1.2–2.0 ppm appears after addition of decane (Fig. 14). There is certain content of WAW in the nanooxide systems in the chloroform media. The main reason of the WAW appearing is the formation of branched 3D clusters of water located in narrow voids. Weakly polar (chloroform) or nonpolar (decane) co-adsorbates are immiscible with water and their molecular sizes are larger than that of water. Therefore, they can displace water into very narrow voids where they cannot be located. The number of such narrow voids increases for cAST due to nanoparticle decomposition. Therefore, displacement effect of decane onto water is stronger for cAST than that for gAST or AST (Fig. 15 *b*).

Confined space effects are characteristic not only for low-molecular weight compounds such as water, decane, decanol, *etc.* but also for liquid polymers such as PDMS [7]. Preheating leads to disordering of supramolecular structures of alone PDMS which prevent observation of mobile polymers (Fig. 16). The temperature dependences of relative intensity of ^{1}H NMR signal differ for individual PDMS initial and preheated at 420 K for 20 min (Fig. 16 *b*). The I/I_0 value corresponds to a

weight fraction of liquid PDMS. The mentioned difference can be explained by additional disordering of PDMS supramolecular structures [7] during heating at 420 K that slows down the PDMS freezing during subsequent cooling; *i.e.* this disorder is partially irreversible. The ^{1}H NMR signal width is narrow (Fig. 16 *a*) that allows us to observe a small upfield shift of δ_H up to –0.1 ppm upon cooling from 280 to 210 K. Subsequent heating gives a downfield shift toward practically the same δ_H values at the same temperatures. There is a hysteresis loop for signal intensity (Fig. 16 *b*). A significant decrease in intensity of PDMS signal occurs during cooling from 240 to 220 K (Fig. 16 *b*), corresponding to the melting point of Oxane 1000 (≈231 K). However, complete freezing of PDMS is not observed even at 210 K. During heating, melting of a part of a frozen PDMS fraction occurs at $T > 250$ K. However, according to DSC data, melting endotherm is located at ~233 K. The hysteresis loop is narrower for preheated PDMS than for initial one due to disordering of supramolecular PDMS structures.

Similar effects at the interfaces depend on the type of adsorbent binding the PDMS due to changes in confined space effects (Figs. 17–19). The temperature behavior of PDMS depends on the surroundings. Confined space effects can be analyzed for PDMS bound to silica gel Si–100 and nanosilica PS400. One can assume that both mesopores and macropores of silicas can be accessible of PDMS molecules. Effect PS400 on PDMS is stronger than that of PS300 or Si–100 since PS400 is composed of smaller and stronger aggregated nanoparticles than PS300 and PS400 stronger immobilizes PDMS than Si–100 because of greater S_{BET}. In contrast to the upfield shift for PDMS alone with decreasing temperature (Fig. 16 *a*), PDMS adsorbed onto silica gel demonstrates a downfield shift with decreasing temperature (Fig. 17 *a*). The spectra of PDMS bound to nanosilica PS400 have a similar shape. The ^{1}H NMR spectra were recorded for PDMS/silica samples equilibrated at 293 K for a week (labeled as "initial") and then these samples were heated at 420 K for 1 h (labeled as "preheated") and measured after preheating.

Comparison of relative intensity curves for PDMS alone (Fig. 16 *b*) and adsorbed onto silicas (Fig. 17 *b–d*) suggests that PDMS molecules become solid-like at temperatures higher than T_f (freezing point) for bulk PDMS. Typically, the freezing point depression is observed for low-molecular weight adsorbates located in pores, and this effect increases with decreasing pore size [7–18]. For adsorbed polymers, this picture is more complex, since a polymer fraction remains liquid at $T < T_f$ but another fraction remains frozen at $T > T_m$ (melting point). It is possible that freezing occurs for an interfacial layer of adsorbed polymer at $T > T_m$. The next layers of the polymer located in pores can be in unfrozen (mobile) state at $T < T_f$. Notice that the hysteresis loops of ^{1}H NMR signal intensity are observed for smaller adsorbates such as hydrophobic *n*-decane bound to silica gel and nanosilica.

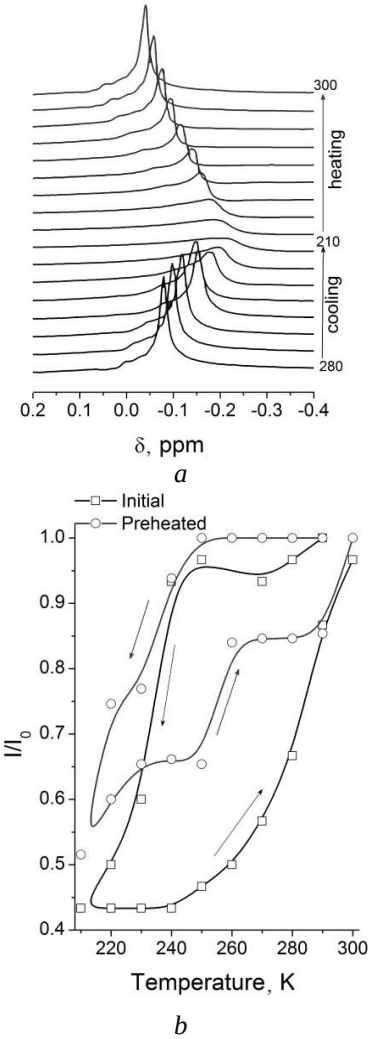

Fig. 16. (*a*) ^{1}H NMR spectra of individual PDMS (Oxane 1000) recorded at different temperatures during cooling and subsequent heating (initial sample); and (*b*) relative intensity (normalized by dividing of current intensity by I_0 of signal recorded at 290 K) of ^{1}H NMR signals for PDMS initial and preheated at 420 K for 20 min

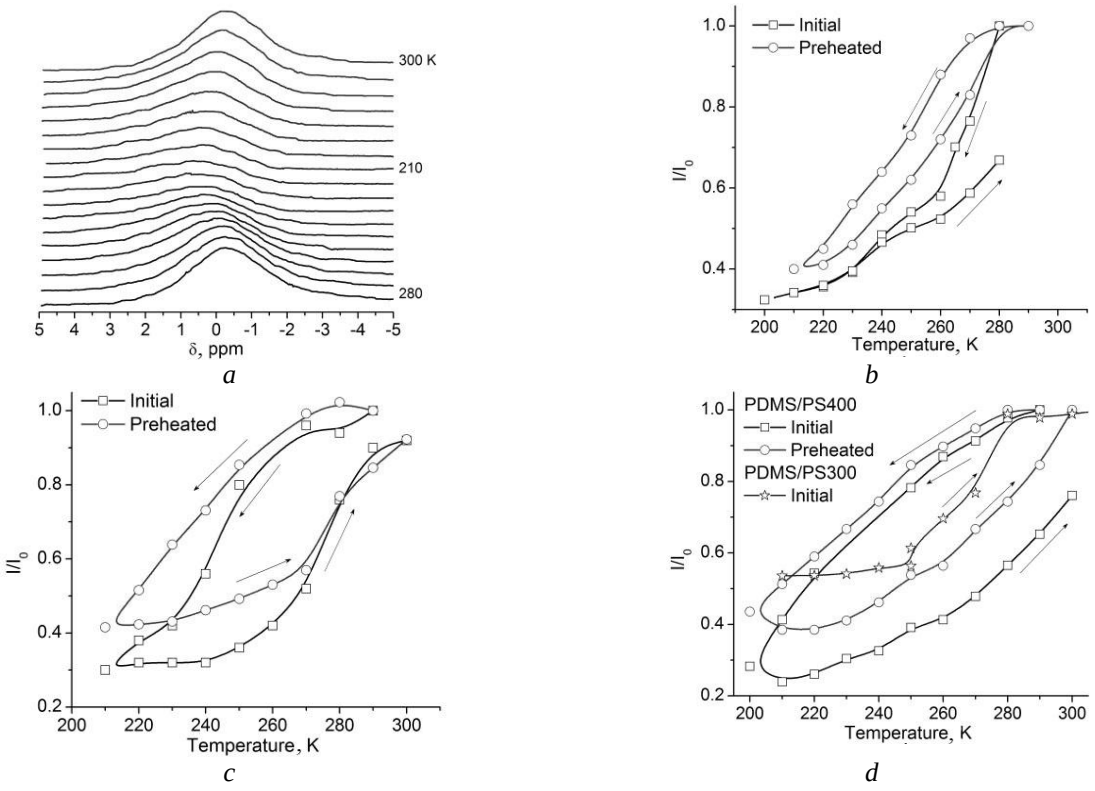

Fig. 17. (*a*) ^{1}H NMR spectra of PDMS (33.3 wt. %) bound to silica gel Si–100 (preheated sample), and changes in relative intensity of ^{1}H NMR signal of CH_3 groups of PDMS adsorbed onto (*b*) silica gel (0.5 g PDMS per gram of Si–100), (*c*) 8 wt. % PS400 in PDMS, and (*d*) PS400 : PDMS or PS300 : PDMS = 1 : 1 for initial and preheated samples

To compare the effects of different sizes of nanoparticles and time of equilibration of PDMS/nanosilica, PDMS/PS300 was also studied (Fig. 17 *d*). Nanosilica PS300 is composed of larger nanoparticles (average $d = 9.2$ nm) than PS400 ($d = 6.7$ nm). Therefore, the surface area of contact of the PDMS molecules with silica nanoparticles in PDMS/PS300 should be smaller than that in PDMS/PS400. This leads to a curve which is closer to that for initial PDMS alone (Fig. 16 *b*) than the curve for PDMS/PS400. Consequently, the relaxation of PDMS is deeper due to a smaller effect of PS300 than that of PS400. The heating rate was the same (5 K/min) for PDMS/PS300 but the equilibration time at a certain temperature was longer: 10 min (instead of 7 min used for PDMS/PS400) at 210 K < T < 250 K for each temperature point, then 30 min (an intensity step observed) and 10 min for subsequent points. Changes in the heating regime lead to certain changes in the intensity curve due to deeper relaxation of the PDMS structure.

The low-temperature ^{1}H NMR spectroscopy used here gives information of the behavior of PDMS with respect to phase transition between liquid and solid-like fractions. Additional information on the temperature behavior of PDMS interacting with different silicas can be obtained using the DSC method. According to the DSC data, the crystallization temperature (T_c) for the sample with 33.3 wt. % PDMS/silica gel is about 177 K during the first scan (Fig. 18 *a*). During the second scan, T_c is about 188 K but this feature is much weaker than that during the first scan. This effect could be explained by disordering supramolecular structure of PDMS macromolecules bound to silica that remains during the second scan.

For PDMS adsorbed in pores of silica gel with the average diameter $d_p \approx 14$ nm (Table 1) similar to the size of typical lamellar structures of PDMS (~10 nm) [29], the melting endotherm is well seen at 227 K for both scans (Fig. 18 *a*) in contrast to that for the PDMS/PS400 system with a very small endotherm observed only upon the first scan (Fig. 18 *b*). This effect can be due to much stronger disordering effect of small nanoparticles of PS400 onto PDMS supramolecular structure than that of silica gel with relatively broad mesopores where

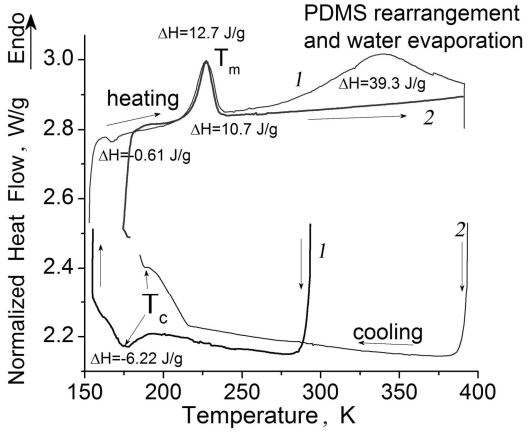

a

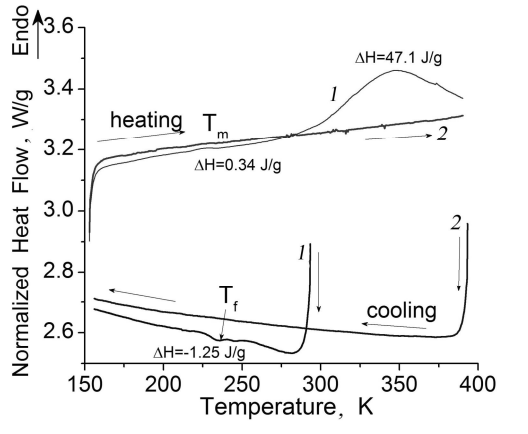

b

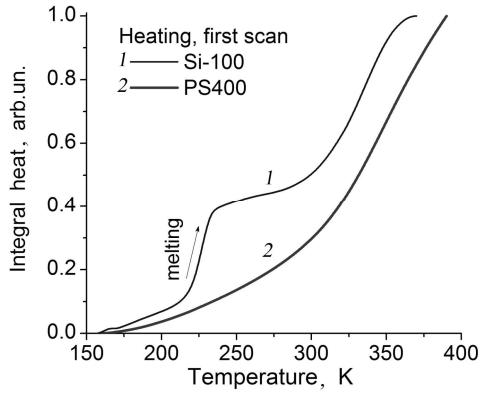

c

Fig. 18. Results of the first (*1*) and the second (*2*) DSC scans for PDMS (33.3 wt. %) bound to (*a*) silica gel Si–100 and (*b*) nanosilica PS400 at cooling-heating rate of 10 K/min; (*c*) integral heat as a function of temperature Φ(*T*) (with subtraction of a nonlinear baseline and normalization to unit) for endo-effects (heating, melting) for PDMS (*1*) confined in pores of Si–100 or (*2*) bound to non-porous PS400 nanoparticles

the PDMS structure can be close to that in the bulk PDMS. These DSC results are in agreement with the NMR data showing the stronger effects of nanosilica than silica gel on the temperature behavior of PDMS. During the first cooling-heating scan, there is a broad endotherm at 273–393 K (Fig. 18) which can be due to several processes [54–61]. Water evaporation can contribute this endotherm but this effect can be small, since the water content in both systems is small < 0.5 wt. %.

In the case of PDMS (33.3 wt. %) bound to nanosilica surface, the melting endotherm peak at 233 K is very small during the first scan (Fig. 18 *b*), and it is practically absent during the second heating run. Additionally, the crystallization exotherm (around 183 K) is absent. However, a small exotherm is observed at 233 K during the first cooling run. This can be due to freezing a small portion of PDMS and/or water bound in narrow nanopores of PS400 which are poorly accessible for PDMS macromolecules. Notice that the broad endotherm at 300–400 K observed during the first scan is larger for PDMS/PS400 (ΔH = 47 J/g) than that for PDMS/Si–100 (ΔH = 39 J/g). This difference can be caused by stronger interactions of the PDMS molecules with the open PS400 surface than that with the silica surface in pores of Si–100. Despite the PDMS amount was much lower (~0.35 cm^3 per gram of silica) than the pore volume of Si–100 (V_p = 1.23 cm^3/g), a film of PDMS was observed at a surface of Si–100 particles. The difference in the morphology of silicas causes a significant difference in the curves of integrated heat flow (determined by Eq. (2)) during heating (endo-effects due to melting) of PDMS bound to Si–100 and PS400 (Fig. 18 *c*), since the PDMS/Si–100 curve has a significant step at 220–230 K in contrast to a smooth curve for PDMS/PS400 (Fig. 18 *c*). This step for PDMS/Si–100 in not vertical because of certain nonuniformity of PDMS with respect to both molecular weight and supramolecular structure of PDMS located in pores of different sizes and out of pores.

Theoretical calculations of the ^{1}H NMR spectra of PDMS fragments (7, 18 or 36 units) free and bound in a pore or out of a pore of silica nanoparticle (Fig. 19) show the effects of both a silica surface (in pore or out of pore) and co-adsorbed water. For PDMS located in the pore, the downfield shift is greater than that for PDMS placed out of the pore (Fig. 19, curves *6* and *7*). For PDMS located in a dry pore, there is the upfield shift (curves *5* and *8*) in comparison with PDMS

located in a hydrated pore (curves *6*, *7*, and *9*) due to enhanced van-der-Waals and electrostatic interactions with surroundings (both silica and water). PDMS in a liquid state (curve *1*) is also characterized by the downfield shift in comparison with individual molecule without neighbors (curves *3* and *4*) due to the effects of the surroundings. Notice that the interaction energy between two PDMS fragments (each with three units) calculated using the DFT wB97XD/6–31G(d,p) method (with HF/6–31G(d,p) geometry) is $\Delta E_t = -9.4$ kJ/mol. However, according to calculation of these two fragments using the Morokuma method by HF/6–31G(d,p), contribution of electrostatic energy is 46.9 % due to interactions of the H atoms of the CH_3 group of a molecule with the O atom in the Si–O–Si bridge of another molecule. This interaction causes a certain polarization of the bonds (H charge increases in the complex from 0.132 to 0.145 a.u. and $q_O = -0.634$ and –0.636 a.u., respectively) and the shielding of protons decreases. This explains the downfield shift of PDMS in the liquid state in comparison with individual PDMS molecules.

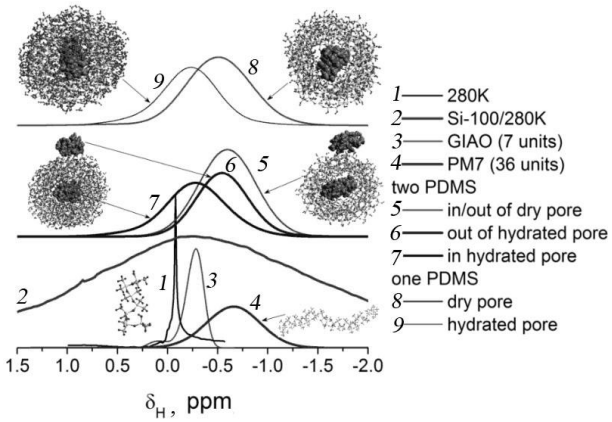

Fig. 19. Experimental ^{1}H NMR spectra of PDMS alone (curve *1*) and adsorbed onto Si–100 (0.5 g/g PDMS) (curve *2*) at 280 K, and theoretically calculated spectra of PDMS alone (7 units) by GIAO/B3LYP/6–31G(d,p) (curve *3*), and PM7 (with full optimization of geometry) with the correlation function $\delta_H = -5.96214 + 33.7732q_H$ (q_H is the atom H charge) for PDMS alone (36 units) (curve *4*), two PDMS molecules (each of 18 units) bound into pore and out of dry pore (curve *5*), out of (curve *6*) and in (curve *7*) hydrated (517 H_2O) pore of silica particle (1624 atoms), one PDMS molecule (18 units) in dry pore (curve *8*) or hydrated pore (curve *9*)

CONCLUSIONS

Combined NMR/DSC/thermoporometry/nitrogen adsorption/quantum chemistry analysis of the temperature and interfacial behavior of *n*-decane, water, 1-decanol and PDMS bound to nanosilica and silica gels shows that a portion of decane, decanol or PDMS remains frozen (quasi-solid) at temperature higher than the freezing point of bulk liquids during heating of samples. Additionally, a fraction of adsorbates remains unfrozen at temperatures below the freezing point during cooling due to the confined space effects. However, freezing and melting curves don't coincide and the hysteresis loop width depends on the NMR (or DSC) experiment conditions and the characteristics of both adsorbents and adsorbates.

For *n*-decane adsorbed onto silica gels Si–40, Si–60 and Si–100, two-four freezing or melting peaks are observed on the DSC thermograms over the 170–300 K range during cooling or heating of samples that depends on the pore size distribution of silicas and the amount of decane. Integrated heat flow curves *vs.* temperature demonstrate the hysteresis loops similar to the effects observed by the NMR method; however, the shapes of the hysteresis loops differ because of the difference in the observed effects: changes in molecular mobility (NMR) or absorption (melting) and release (freezing) of heat (DSC). According to ^{1}H NMR data, a portion of *n*-decane, which is in quasi-crystalline state characterized by fast molecular exchange (short transverse relaxation time) and not observed in the NMR spectra, is greater during heating of samples than a portion of decane frozen during cooling at temperature close to the freezing point of bulk liquid (T_f). A similar effect appearing

in the DSC endotherms for samples heated at the same heating rate is smaller than that in the NMR measurements due to different excess in the decane amounts and the difference in the phenomena studied by the ^{1}H NMR (changes in molecular mobility with temperature) and DSC (release or absorption of heat with decreasing or increasing temperature) methods. The enhanced confined space effects for nanosilica PS400 compacted toward twice greater bulk density (0.15 g/cm^3 instead of 0.07 g/cm^3 for the initial PS400) result in an increase in a portion of unfrozen *n*-decane at $T > T_f$. In the case of a small content of water co-adsorbed with *n*-decane (of a large content > V_p), water displaced by decane into narrower pores where it cannot form large structures. Therefore, this water is weakly associated water.

The studied regularities in the temperature and interfacial behavior of water and *n*-decane, 1–decanol or PDMS co-adsorbed onto different silicas can be used to explain features of the work and the efficiency of adsorbents applications at various temperatures and concentrations of adsorbates.

A portion of decane or decanol remains frozen (quasi-solid) at temperature higher than the freezing point of bulk liquids during heating of samples. A fraction of adsorbates remains unfrozen at temperatures below the freezing point during cooling due to the confined space effects. Two fractions of PDMS (liquid and solid-like, frozen) co-exist over a broad temperature range spreading toward both sides from the melting point. The broadening of the range of melting of PDMS depends on the pore size distribution, and it is minimal for silica gel Si–100 with broader pores. Freezing and melting curves do not coincide and the hysteresis loop width depends on the NMR or DSC experiment conditions.

The temperature behavior of PDMS differs for polymers alone or bound to silica gel Si–100 and nanosilica PS400. The low-temperature ^{1}H NMR spectroscopy shows that two fractions of PDMS (liquid and solid-like, frozen) co-exist over a broad temperature range spreading toward both sides from the PDMS melting point. The transverse relaxation times of protons in methyl groups strongly differ for liquid and solid-like PDMS that allows quantitative estimation of contributions of both fractions *vs*. temperature. The cooling-heating of PDMS and PDMS/silica samples gives the hysteresis loop for intensity of ^{1}H NMR signals. The loop width depends on the surrounding (bulk PDMS or PDMS adsorbed on a silica surface) and confined space effects (silica gel or nanosilica). It also strongly differs for initial and samples preheated at 420 K. The observed differences can be explained by various order or disorder of supramolecular structures of PDMS alone, adsorbed and preheated. DSC measurements of polymers (33.3 wt. %) bound to silica gel and nanosilica show that bound PDMS is characterized by different temperature behavior on the first and second cooling-heating scans and this behavior contrasts for silica gel and nanosilica. For PDMS/silica gel, supramolecular structures can be more ordered than that for PDMS/nanosilica. Both melting endotherm and crystallization exotherm are observed for PDMS/silica gel. However, both thermal features are much weaker for PDMS/nanosilica and observed only during the first temperature scan. This difference can be explained by stronger interactions of polymers with silica nanoparticles than with a surface in pores of silica gel because penetrating of macromolecules into relatively narrow and long pores (since silica gel beads have 0.2–0.5 mm in diameter) can be more difficult than mixing nanoparticles with PDMS molecules.

Acknowledgment. The work was supported by the FP7-PEOPLE-IRSES, projects No 230790 and 612484.

Міжфазна поведінка низько- та високомолекулярних сполук в залежності від температури і ефектів обмеженого простору

В.М. Гунько, В.В. Туров, В.І. Зарко, О.В. Гончарук, О.С. Ремез, R. Leboda, J. Skubiszewska-Zięba

Інститут хімії поверхні ім. О.О. Чуйка Національної академії наук України
вул. Генерала Наумова, 17, Київ, 03164, Україна, vlad_gunko@ukr.net
Університет імені Марії Кюрі-Склодовської, хімічний факультет
пл. Марії Кюрі-Склодовської, 3, Люблін, 20031, Польща

Міжфазна та температурна поведінка води, н-декану, деканолу, полідиметилсилоксану (ПДМС), зв'язаних нанооксидами, вихідними і після кріожелювання при високому тиску, та силікагелями проаналізована за допомогою низькотемпературної ^{1}H ЯМР спектроскопії (з використанням статичних зразків для спостереження тільки рухливих адсорбатів), диференційної скануючої калориметрії (ДСК), термопорометрії й методів квантової хімії. Як ЯМР, так і ДСК результати вказують на те, що при нагріванні заморожених зразків частина органічних сполук чи ПДМС лишається замороженою при температурі вище точки плавлення об'ємної рідини, а при охолодженні частина адсорбату лишається у рідкому стані при температурі нижче точки замерзання. Ці ефекти залежать від типу адсорбату і розподілу пор за розміром адсорбенту. Розширення інтервалу замерзання/плавлення спостерігається для ПДМС і декану, локалізованих у порах силікагелю або між наночастинками пірогенних оксидів. Цей ефект мінімальний для силікагелю Si–100, який має широкі мезопори.

***Ключові слова**: нанооксиди, силікагель, кріонанооксиди, міжфазні явища, ефекти обмеженого простору, зниження точки замерзання, охолодження/нагрівання, гістерезисні ефекти*

Межфазное поведение низко- и высокомолекулярных соединений в зависимости от температуры и эффектов ограниченного пространства

В.М. Гунько, В.В. Туров, В.И. Зарко, Е.В. Гончарук, О.С. Ремез, R. Leboda, J. Skubiszewska-Zięba

Институт химии поверхности им. А.А. Чуйко Национальной академии наук Украины
ул. Генерала Наумова, 17, Киев, 03164, Украина, vlad_gunko@ukr.net
Университет имени Марии Кюри-Склодовской, химический факультет
пл. Марии Кюри-Склодовской, 3, Люблин, 20031, Польша

Межфазное и температурное поведение воды, н-декана, деканола, полидиметилсилоксана (ПДМС), связанных нанооксидами, исходными и после криожелирования при высоком давлении, и силикагелями проанализирована с помощью низкотемпературной ^{1}H ЯМР спектроскопии (с использованием статичных образцов для наблюдения только подвижных адсорбатов), дифференциальной сканирующей калориметрии (ДСК), термопорометрии и методов квантовой химии. Как ЯМР, так и ДСК результаты указывают на то, что при нагревании замороженных образцов часть органических соединений или ПДМС остается замороженной при температуре выше точки плавления объемной жидкости, а при охлаждении часть адсорбата остается в жидком состоянии при температуре ниже точки замерзания. Эти эффекты зависят от типа адсорбата и распределения пор по размерам адсорбента. Расширение интервала замерзания/плавления наблюдается для ПДМС и декана, локализованных в порах силикагеля или между наночастицами пирогенных оксидов. Этот эффект минимальный для силикагеля Si–100, который имеет широкие мезопоры.

***Ключевые слова**: нанооксиды, силикагель, кронанооксиды, межфазные явления, эффекты ограниченного пространства, снижение точки замерзания, охлаждение/нагревание, гистерезисные эффекты*

REFERENCES

1. *Iler R.K.* The Chemistry of Silica, Wiley, Chichester, 1979, 886 p.
2. *Legrand A.P.* (Ed.) The Surface Properties of Silicas, Wiley, New York, 1998, 470 p.
3. *Hubbard A.T.* (Ed.) Encyclopedia of Surface and Colloid Science, New York, Marcel Dekker, 2002, 5667 p.
4. *Bergna H.E.* (Ed.) Colloidal Silica: Fundamentals and Applications, Salisbury, Taylor & Francis LLC, 2005, 953 p.
5. *Fendler J.H.* (Ed.) Nanoparticles and Nanostructured Films, Weinheim, Wiley-VCH, 1998, 490 p.
6. *Blitz J.P., Gun'ko V.M.* (Eds.) Surface Chemistry in Biomedical and Environmental Science, Springer, Dordrecht, NATO Science Series II: Mathematics, Physics and Chemistry, 2006, 434 p.
7. *Gun'ko V.M., Turov V.V.* Nuclear Magnetic Resonance Studies of Interfacial Phenomena, Boca Raton, CRC Press, 2013, 1040 p.
8. *Gun'ko V.M., Morozova L.P., Turova A.A. et al.* Hydrated phosphorus oxyacids alone and adsorbed on nanosilica. J. Colloid Interface Sci., 368 (2012) 263.
9. *Gun'ko V.M., Turov V.V., Turov A.V.* Hydrogen peroxide - water mixture bound to nanostructured silica, Chem. Phys. Lett., 531 (2012) 132.
10. *Gun'ko V.M., Savina I.N., Mikhalovsky S.V.* Cryogels: Morphological, structural and adsorption characterisation. Adv. Colloid Interface Sci., 187–188 (2013) 1.
11. *Gun'ko V.M., Turov V.V., Krupska T.V. et al.* Interfacial behavior of silicone oils interacting with nanosilica and silica gels. J. Colloid Interface Sci., 394 (2013) 467.
12. *Gun'ko V.M., Sulym I.Y., Borysenko M.V., Turov V.V.* Interfacial behavior of water bound to zirconia/nanosilica with adsorbed poly(dimethylsiloxane). Colloids Surf. A: Physicochem. Eng. Aspects. 426 (2013) 47.
13. *Turov V.V., Gun'ko V.M., Zarko V.I. et al.* Interfacial behavior of *n*-decane bound to weakly hydrated silica gel and nanosilica over a broad temperature range, Langmuir, 29 (2013) 4303.
14. *Gun'ko V.M., Turov V.V., Leboda R. et al.* Confined space effects driving to heterogenization of solutions at the interfaces, Adsorption, 19 (2013) 305.
15. *Gun'ko V.M.* Modeling of interfacial behavior of water and organics, J. Theoret. Comput. Chem., 12 (2013) 1350059.
16. *Gun'ko V.M., Turov V.V., Turova A.A. et al.* Interactions of poly(dimethylsiloxane) with nanosilica and silica gel upon cooling-heating, J. Colloid Interface Sci. 426 (2014) 48.
17. *Gun'ko V.M., Turov V.V., Zarko V.I. et al.* High-pressure cryogelation of nanosilica and surface properties of cryosilicas, Colloids Surf. A: Physicochem. Eng. Aspects, 436 (2013) 618.
18. *Gun'ko V.M., Turov V.V., Zarko V.I. et al.* Cryogelation of individual and complex nanooxides under different conditions, Colloids Surf. A: Physicochem. Eng. Aspects, 456 (2014) 261.
19. *Gregg S.J., Sing K.S.W.* Adsorption, Surface Area and Porosity, London, Academic Press, 1982, 303 p.
20. *Gun'ko V.M.* Composite materials: textural characteristics, Applied Surface Sci., 307 (2014) 444.
21. *Provencher S.W.* Constrained regularization method for inverting data, Comp. Phys. Comm., 27 (1982) 213.
22. *Nguyen C., Do D.D.* A new method for the characterization of porous materials, Langmuir, 15 (1999) 3608.
23. *Gun'ko V.M., Do D.D.* Characterization of pore structure of carbon adsorbents using regularization procedure. Colloids Surf. A: Physicochem. Eng. Aspects, 193 (2001) 71.
24. *Gun'ko V.M., Mikhalovsky S.V.* Evaluation of slitlike porosity of carbon adsorbents, Carbon, 42 (2004) 843.
25. *Frisch M.J., Trucks G.W., Schlegel H.B. et al.* Gaussian 09, Revision D.01, Gaussian, Inc., Wallingford CT, 2013.
26. *Stewart J.J.P.* MOPAC 2012, Colorado Springs, CO: Stewart Computational Chemistry, USA, http://openmopac.net/, 2014.
27. *Maia J.D.C., Carvalho G.A.U., Mangueira C.P. et al.* GPU linear algebra libraries and GPGPU programming for accelerating MOPAC semiempirical quantum chemistry calculations, J. Chem. Theory Comput., 8 (2012) 3072.
28. *Granovsky A.A.* Firefly version 8.1, www http://classic.chem.msu.su/gran/gamess/index.html.

Received 05.06.2014, accepted 17.09.2014